CHAPTER 4

RESULTS AND DISCUSSIONS

In this chapter, the measurement of structural, optical, electrical and photocatalytic properties of ZnO and ZnO–TiO_2 coupled thin films prepared by sparking process are presented. Morphologies of the films were characterized by using atomic force microscopy (AFM) and scanning electron microscopy (SEM). Structural properties were characterized by X-ray diffraction and Raman spectroscopy. Optical properties were studied by ionoluminescence, and UV-vis spectroscopy. Otherwise, the photocatalytic property was studied by the concentration reducing, using methelene blue (MB) drop on the films under the sunlight.

4.1 Vertical tips alignment sparking

4.1.1 Effect of electrode polarity

Optical microscope images of the conical tip after the sparking occurred are shown in fig. 4.1, where the conical tip was connected to the capacitor (a) as the anode and (b) as the cathode. While achieving a higher deposition rate, it should be noted that an erosion of the anode tip was clearly seen, whereas the cathode tip was slightly eroded. On the basis of this result, the anodic tip was selected for depositing ZnO nanoparticles (NPs) on quartz substrates.

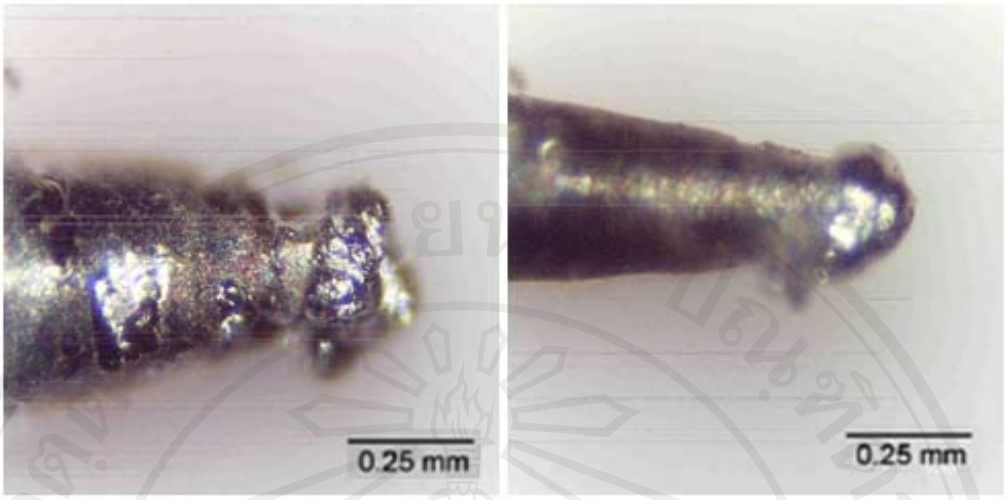

(a) (b)

Fig. 4.1 Optical microscope images of (a) the anode tip and (b) the cathode tip after the sparking occurred. (The original tip was shown in fig. 3.1 (a))

4.1.2 Effect of tip shape

A comparison of AFM images is shown in Fig. 4.2(a), (b) and (c), in which the NPs were prepared by sparking once at 4 kV from the conical tip, the sharp tip and the dull tip, respectively. It is noted that the NPs prepared from the dull tip have the largest average particle sizes, whereas those prepared from the sharp tip and the conical tip have slightly different average sizes.

From the more detailed information from section analysis of Nanoscope IIIa 5.12r3 software, the mean sizes of ZnO NPs prepared from the conical the sharp and the dull tips were approximately 36, 37 and 61 nm in diameter and 17, 12, 15 nm in height, respectively (fig. 4.3). The conical tips have the smallest angle of the cone and radius of curvature so they have the highest field enhance factor and this will be discussed in section 4.5. Therefore, the local electric field of conical tip is the highest so the tip transfer highest energy and produces the smallest nanoparticles.

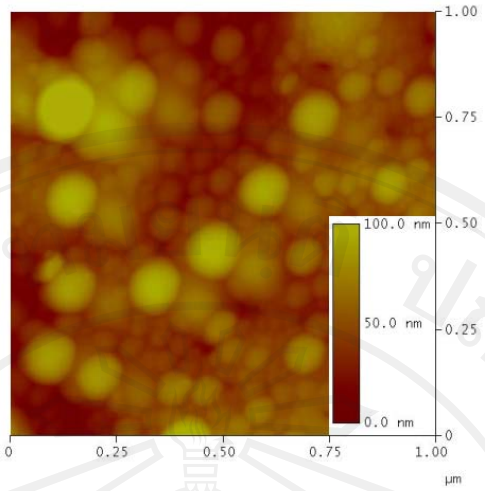

(a)

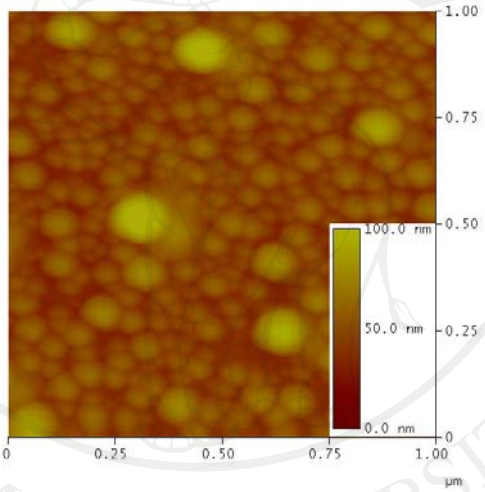

(b)

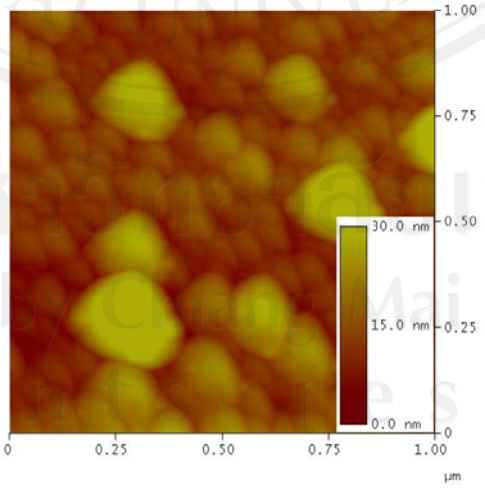

(c)

Fig. 4.2 AFM images of ZnO NPs prepared by sparking once at 4 kV from (a) the conical tip (b) the sharp tip and (c) the dull tip.

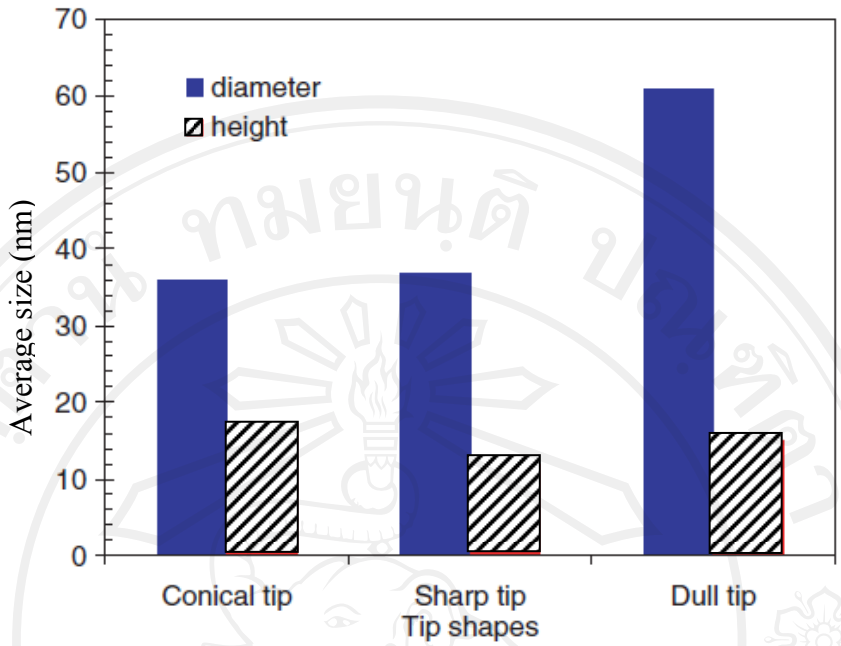

Fig. 4.3 The mean heights and the average diameters of ZnO NPs prepared by sparking once from the different tip shapes at 4 kV**.**

4.1.3 Effect of sparking voltage

As suggested in section 4.1.1, the sharp tip was selected to study the relationship between the strength of applied voltages and the average sizes of the NPs. The result is shown in fig. 4.4.

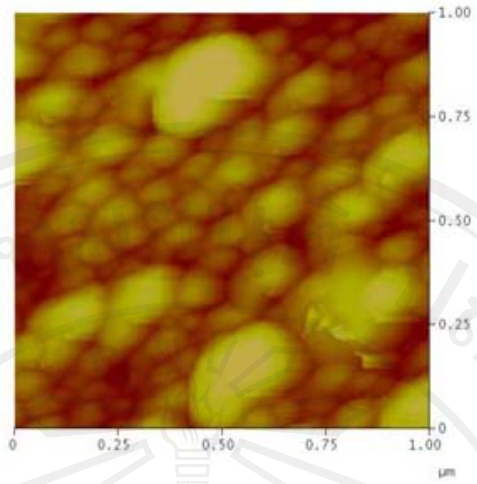

(a)

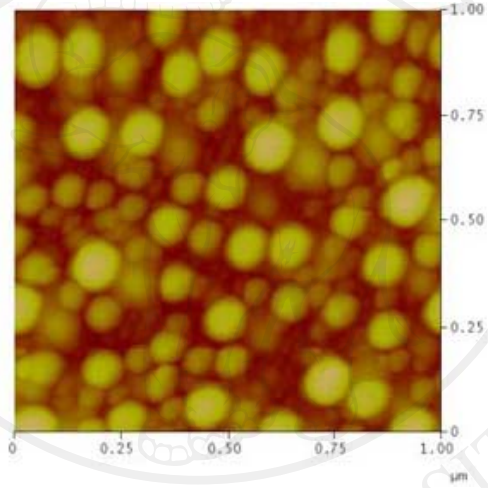

(b)

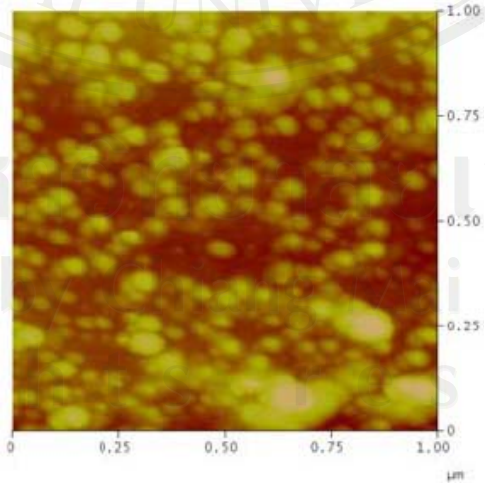

(c)

Fig. 4.4 AFM images of ZnO NPs prepared by sparking once from sharp tip at (a) 2 kV (b) 4 kV and (c) 6 kV.

The average diameters and the average heights prepared at 2, 4 and 6 kV were approximately 41, 36 and 34 nm and 16, 12 and 8 nm, respectively. It is clearly seen that sparking at a voltage of 6 kV has deposited the lowest average particle sizes. Understand that, a high specific surface energy is governed by the associated energy stored in such a system. Since the electric energy stored in a capacitor is $E = ½ CV^2$, sparking at 6 kV supports the lower average sizes of the NPs.

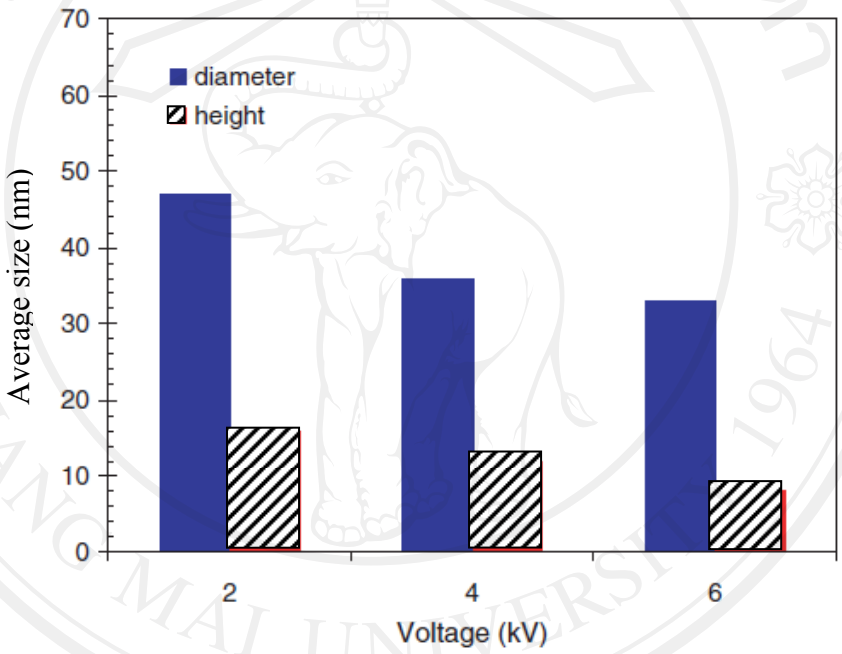

Fig. 4.5 The mean heights and the mean diameters of ZnO NPs prepared by sparking once from the sharp tip at 2, 4 and 6 kV.

4.2 Horizontal tips alignment sparking ZnO nanoparticles thin films

The horizon tip alignment was produced for deposited ZnO nanoparticles thin films on quartz substrate. In order to achieve the smallest sizes, the sharp tip and sparking at high voltage, 10 kV, were considered to be the optimum choice and will be used in this experiment.

4.2.1 Surface morphology as imaged by AFM

AFM images of the sparking thin films are shown in Fig. 4.6 (a) – (d). The root mean square (rms) roughness of 46, 45, 36 and 28 nm and the corresponding grain sizes of 30, 36, 42 and 44 nm were obtained from the as-deposited sample and the samples annealed at 400, 600 and 800 °C, respectively (shown in fig. 4.7).

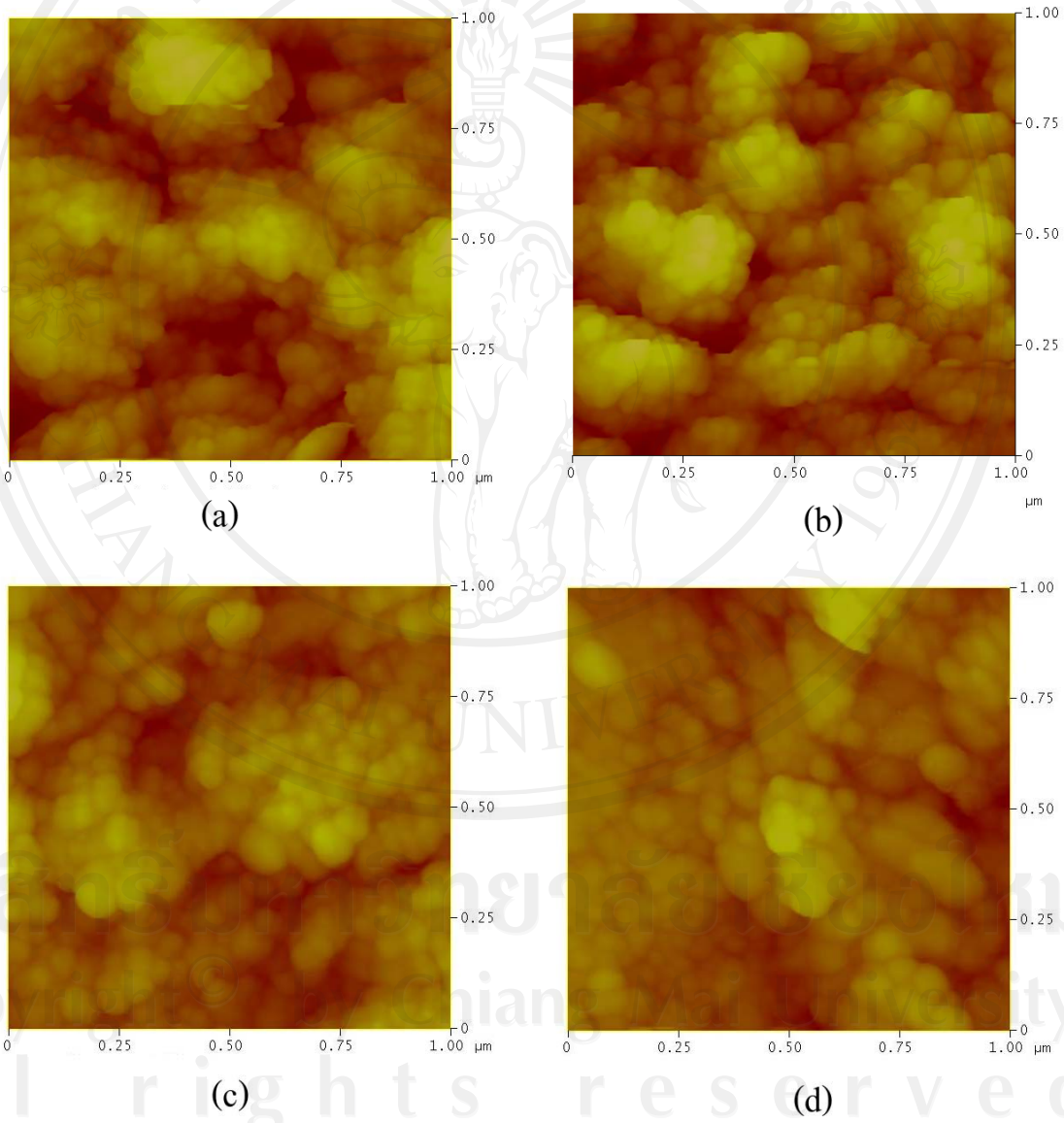

Fig. 4.6 AFM images of ZnO thin films (a) the as-deposited sample and the samples annealed at (b) 400 °C, (c) 600 °C, and (d) 800 °C.

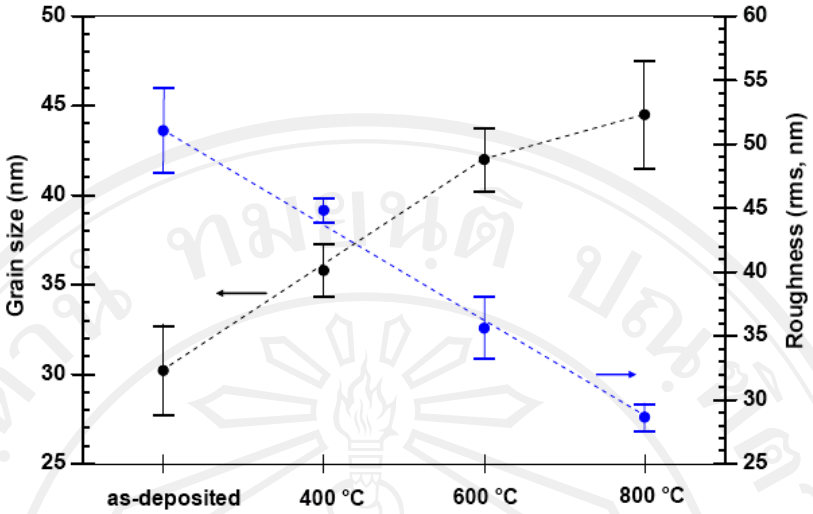

Fig. 4.7 The grain size and the surface roughness of AFM images as functions of the annealing temperature.

4.2.2 Surface morphology and cross-section as imaged by SEM

The surface morphology of the ZnO is shown in fig. 4.8. The films were produced by the pile of the nanoparticles. The primary nanoparticles are nearly spherical particle, having average size of ~ 20 nm, and the nucleation mechanism is explained in section 4.5. The grain sizes obtained from AFM images are slightly larger than those observed from SEM images, due to the broadening effect of the tip shape convolution [59].

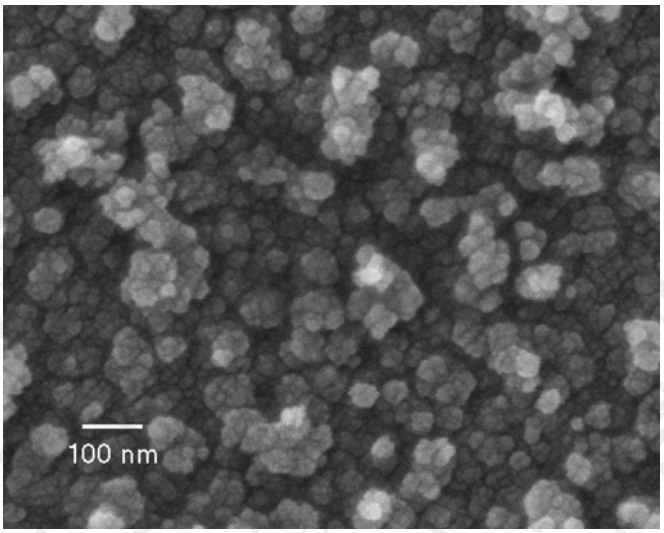

Fig. 4.8 SEM images of as-deposited ZnO nanoparticles thin films.

The corresponding SEM cross-section image, as shown in fig. 4.9, of ZnO thin films after sparking at 50-200 times. Fig. 4.10 displays the film thickness as a function of the sparking number. It is clearly seen that, the film thickness increased linearly from 50 to 200 nm with increasing sparking from 50 to 200 times. In other words, the film deposition rate by sparking process was approximately 1.0 nm/spark.

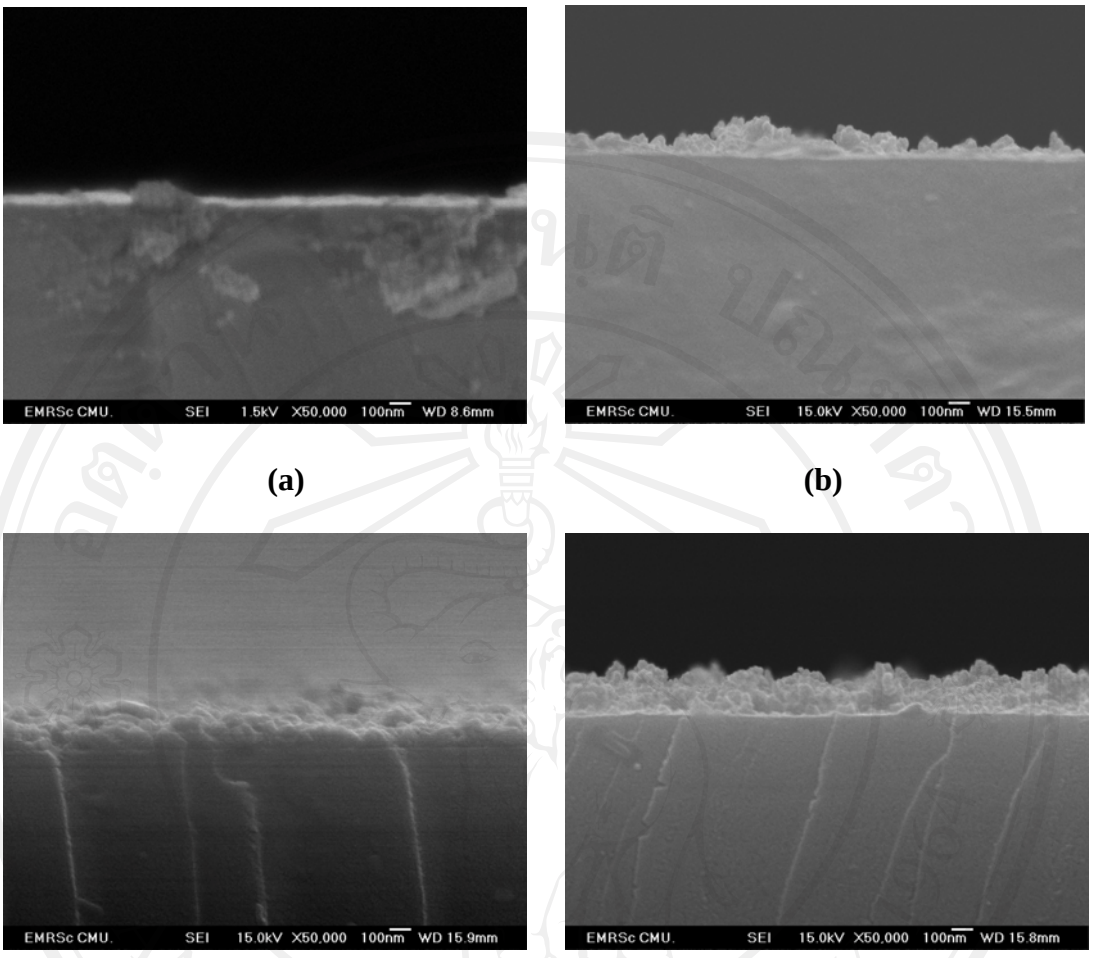

Fig. 4.9 SEM cross section images of the ZnO films sparking number of (a) 50 times, (b) 100 times, (c) 150 times and (d) 200 times.

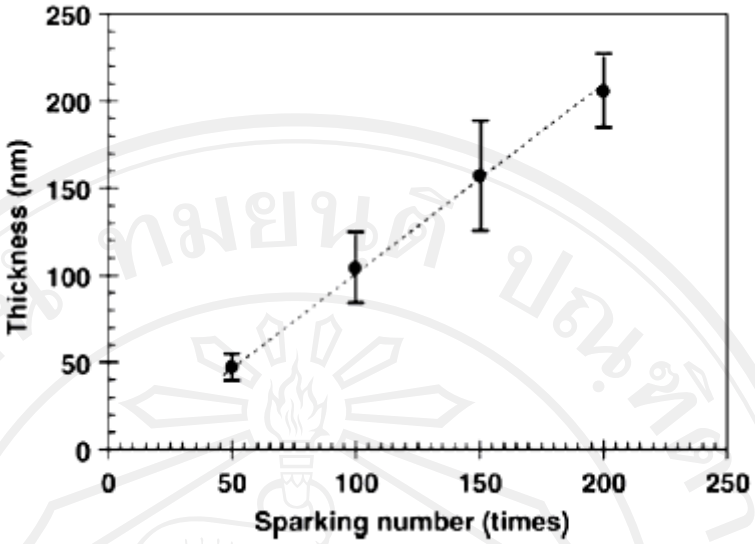

Fig. 4.10 The thickness of the ZnO thin films as a function of the sparking numbers.

4.2.3 X-ray diffraction of sparking ZnO

XRD patterns of sparking ZnO shown in Fig.4.11, exhibit polycrystalline structure of hexagonal wurtzite ZnO. Only a broad peak of amorphous quartz was observed from the as-deposited sample. Diffraction peaks (2θ) of the annealed samples at 31.8°, 34.4°, 36.3° ,47.5°, 56.6°, 62.9°, and 67.8° correspond to (100), (002), (101), (110), (102), (103), and (112) planes, respectively. The peak intensities increased with increasing in the annealing temperature up to 600 °C at which the ZnO films were well crystallized. In other words, the transformation of the amorphous phase to the polycrystalline ZnO films mainly occurred at 600 °C. However, as the annealing temperature increased further up to 800 °C, the intensities of XRD peaks were decreased. It was ascribed to higher oxygen vacancy defects at that temperature.

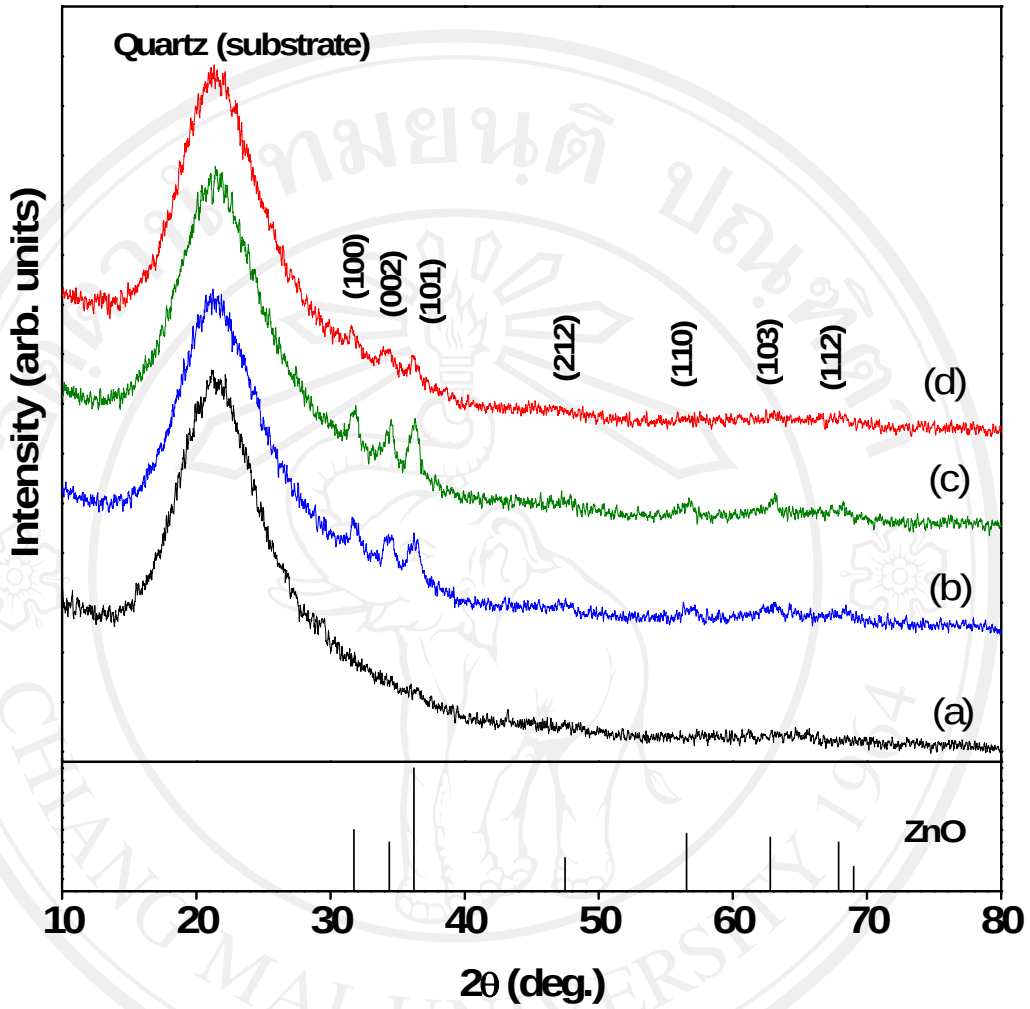

Fig. 4.11 XRD spectra of ZnO thin films of (a) the as-deposited sample and the samples annealed at (b) 400 °C, (c) 600 °C, and (d) 800 °C.

4.2.4 UV–vis spectroscopy

Figure 4.12 shows the transmittance of ZnO thin films. The optical transmittance in the visible region drops with increasing the annealing temperature to the minimum transmittance at 600 °C. Furthermore, the optical transmittance also relate to the film crystallization and orientation, as shown in XRD patterns of fig. 4.11

The increasing of crystallization reduces the optical transmittance because the high crystalline semiconductor can absorb light more than amorphous which is confirmed by absorption spectra, in fig. 4.13. The absorption of light (or generally of electromagnetic radiation) occurs by several mechanisms such as the light-induced vibration of the lattice atoms and cause electron to be excited into higher energy state. Therefore, the films which high crystallization can be absorbed light more than amorphous films.

All spectra are high transparency in visible region and suddenly drop in UV region, around 390 nm, because ZnO is an extremely high-UV-shielding material.

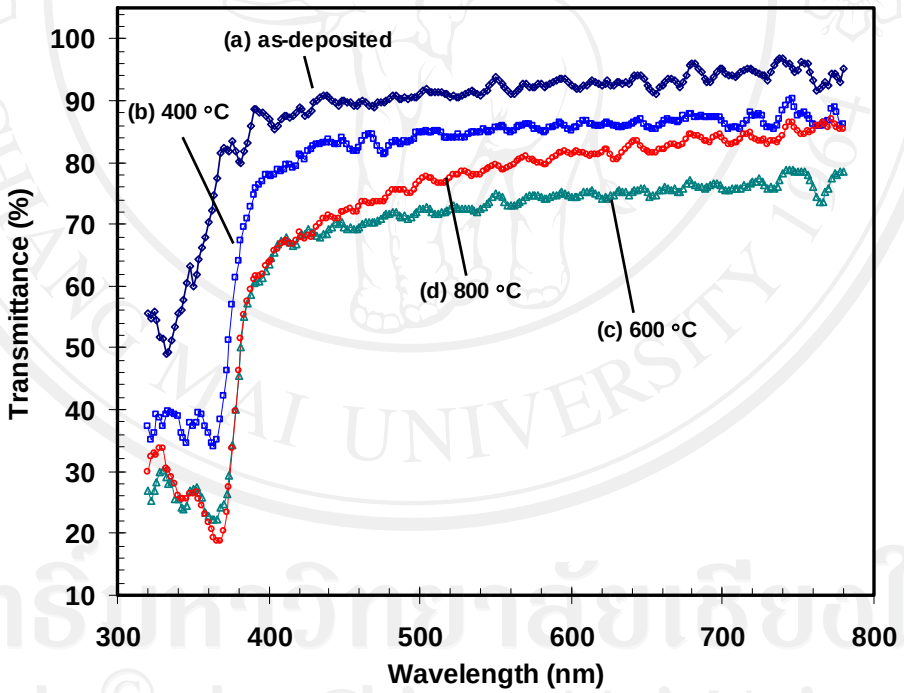

Fig. 4.12 Optical transmittance spectra of ZnO thin films of (a) the as-deposited sample and the samples annealed at (b) 400 °C, (c) 600 °C, and (d) 800 °C.

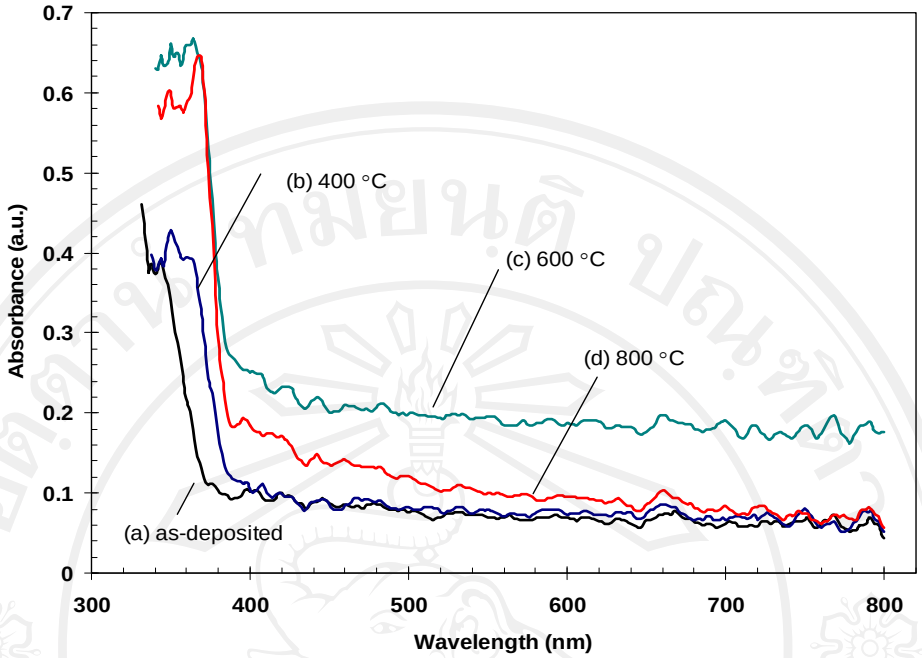

Fig. 4.13 Optical absorption spectra of ZnO thin films of (a) the as-deposited sample and the samples annealed at (b) 400 °C, (c) 600 °C, and (d) 800 °C.

The band gap can be determined from the plot of $(\alpha h\nu)^2$ versus the photon energy hν, (Figs. 4.14-4.16 and table 4.1-4.4 from the extrapolation of the linear portion with the energy axis, where α is the absorption coefficient.

The estimated band gaps and the linear equations of the as-deposited and the annealed samples are shown in Table 4.1-4.3 for $\alpha = \frac{1}{t}\ln\frac{(1-R)}{T}$, $\frac{(1-C)^2}{C}$, and $\ln\frac{1}{T}$, respectively. It is noted that the band gaps determined from the various α were slightly different. The band gap of the as-deposited sample is higher than those of the annealed samples. According to the band gap observed from as-deposited sample, a possible explanation is that the nanoparticles are passivated by an outer thin layer of $Zn(OH)_2$, from moisture in air, in which it increases the energy band gap [60].

The sparking for depositing ZnO nanoparticles in air at room temperature took place in incomplete oxidation and humidity, i.e. the $Zn/ZnO/Zn(OH)_2$ core–shell–shell structure was probably formed. Therefore, an annealing treatment is needed for obtaining good quality of the nanoparticles thin films prepared by sparking method.

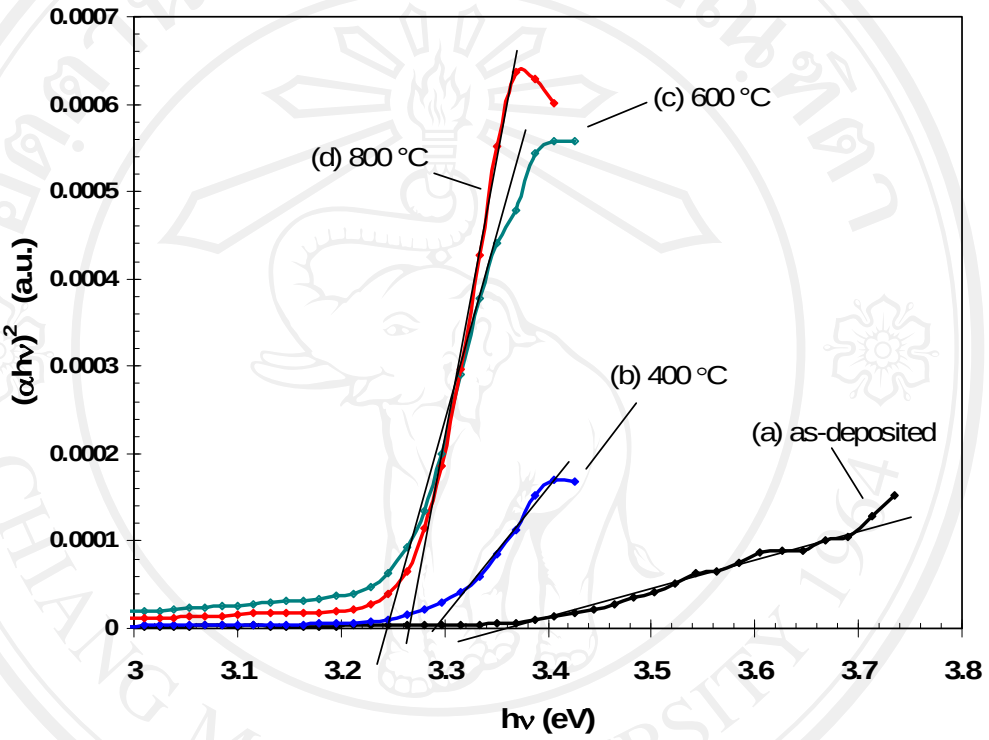

Fig. 4.14 The Tauc's plot for estimation of the energy gaps of the films, $\alpha = \frac{1}{t}\ln\frac{(1-R)}{T}$, where t is film thickness, R is reflectance and T is the transmittance.

Table 4.1 The Tauc' plot for estimated band gap of ZnO films as shown in fig. 4.14, using $\alpha = \frac{1}{t}\ln\frac{(1-R)}{T}$ where t is film thickness, R is reflection and T is transmitance.

Samples	Linear equation	Band Gap (eV) (y-intercept)	coefficient of determination (R^2)
As-deposited	y = 0.000333x – 0.00112	3.36	0.9850
400 °C	y = 0.00138x – 0.00453	3.28	0.9793
600 °C	y = 0.00379x – 0.01229	3.24	0.9891
800 °C	y = 0.00518x – 0.01684	3.25	0.9672

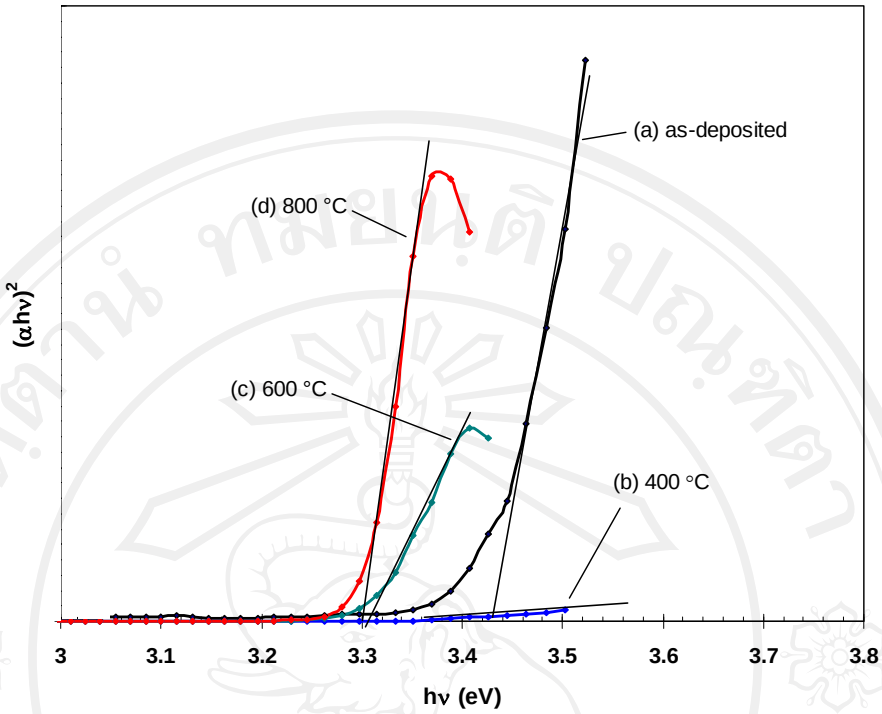

Fig. 4.15 The Tauc's plot for estimation of the energy gaps of the films, $\alpha = \frac{(1-C)^2}{C}$, where $C = 10^{-A}$, A is absorbance.

Table 4.2 The Tauc's plot for estimation of the energy gaps of the films as shown in fig. 4.15, $\alpha = \frac{(1-C)^2}{C}$, where $C = 10^{-A}$, A is absorbance.

Samples	Linear equation	Band Gap (eV) (y-intercept)	coefficient of determination (R^2)
As-deposited	y = 57.10x – 196.76	3.44	0.9702
400 °C	y = 0.78x – 2.65	3.39	0.9545
600 °C	y = 67.97x – 225.68	3.32	0.9564
800 °C	y = 319.32x – 1049.27	3.28	0.8649

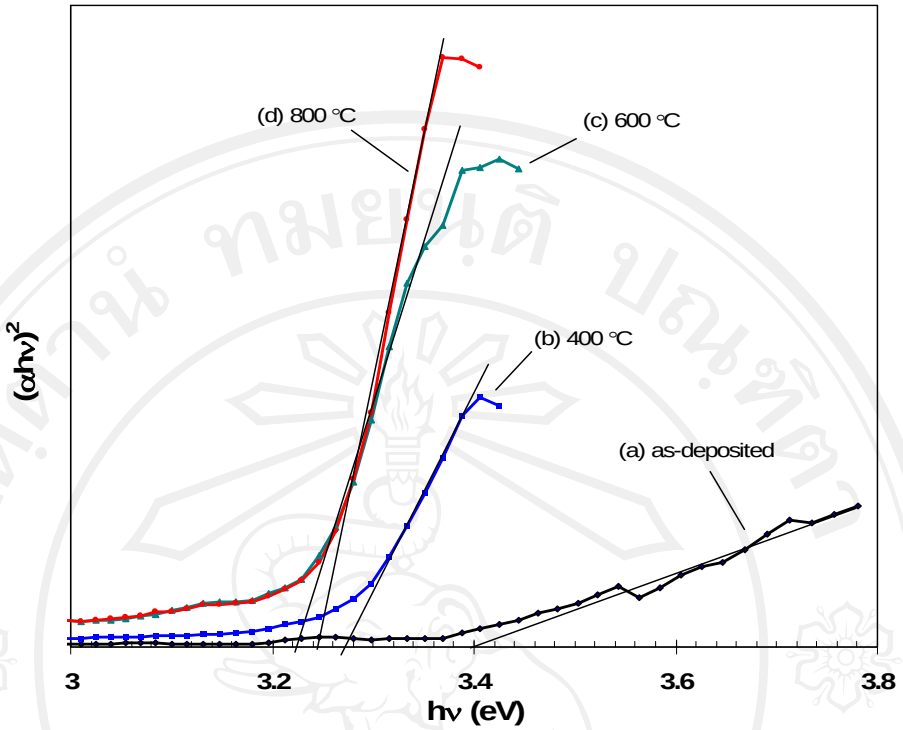

Fig. 4.16 The Tauc's plot for estimation of the energy gaps of the films, $\alpha = \ln \frac{1}{T}$, where T is the transmittance.

Table 4.3 The Tauc's plot for estimation of the energy gaps of the films as shown in fig. 4.16, $\alpha = \ln \frac{1}{T}$, where T is the transmittance.

Samples	Linear equation	Band Gap (eV) (y-intercept)	coefficient of determination (R^2)
As-deposited	y = 18.05x – 60.79	3.36	0.9729
400 °C	y = 97.55x – 318.40	3.26	0.9948
600 °C	y = 191.00x – 615.50	3.22	0.9430
800 °C	y = 253.80x – 822.99	3.24	0.9940

Table 4.4 The band gaps of ZnO samples estimated from different absorption coefficients (α): **t** is the film thickness (nm), **R** is the reflectance, **T** is the transmittance, **C** is the reflection coefficient (**C** = 10^{-A}) and **A** is the absorbance.

Samples	Band gap (eV)		
	$\alpha_1 = \frac{1}{t}\ln\frac{(1-R)}{T}$ [54]	$\alpha_2 = \frac{(1-C)^2}{C}$ [55]	$\alpha_3 = \ln\frac{1}{T}$ [56]
As-deposited	3.36	3.44	3.36
400 °C	3.28	3.39	3.26
600 °C	3.24	3.32	3.22
800 °C	3.25	3.28	3.24

4.2.5 Raman spectroscopy

As being one of the simplest uniaxial crystals, ZnO with wurtzite structure belongs to the $P6_3mc$ space group. For the perfect ZnO crystal, only the optical phonons at Γ point of the Brillouin zone are involved in first-order Raman scattering. Group theory predicts the existence of the following optic modes [61]

$$\Gamma_{opt} = A_1 + 2B_1 + E_1 + 2E_2$$

where both A_1 and E_1 modes are polar and split into transverse optical (A_1 TO and E_1 TO) and longitudinal optical (A_1 LO and E_1 LO) components. E_2 mode consists of two modes of low and high frequency phonons (E_2 low and E_2 high), which are associated with the vibrations of the heavy Zn sublattice and oxygen atoms, respectively. B_1 are infrared and Raman silent mode.

Raman spectra before and after the annealing treatments of ZnO thin films are shown in fig. 4.16. The chemical finger print of the ZnO phase was confirmed by the peaks centered at 332, 440, 580, and 1140 cm^{-1}, which correspond to the second order of Raman scattering, the E (high), the A_1 (LO), and the 2LO modes, respectively [62-63]. However, the peaks centered at 490, 800, and 1068 cm^{-1} are the optical phonon modes of the quartz substrate, of which the peak intensities were likely unchanged by the annealing treatments.

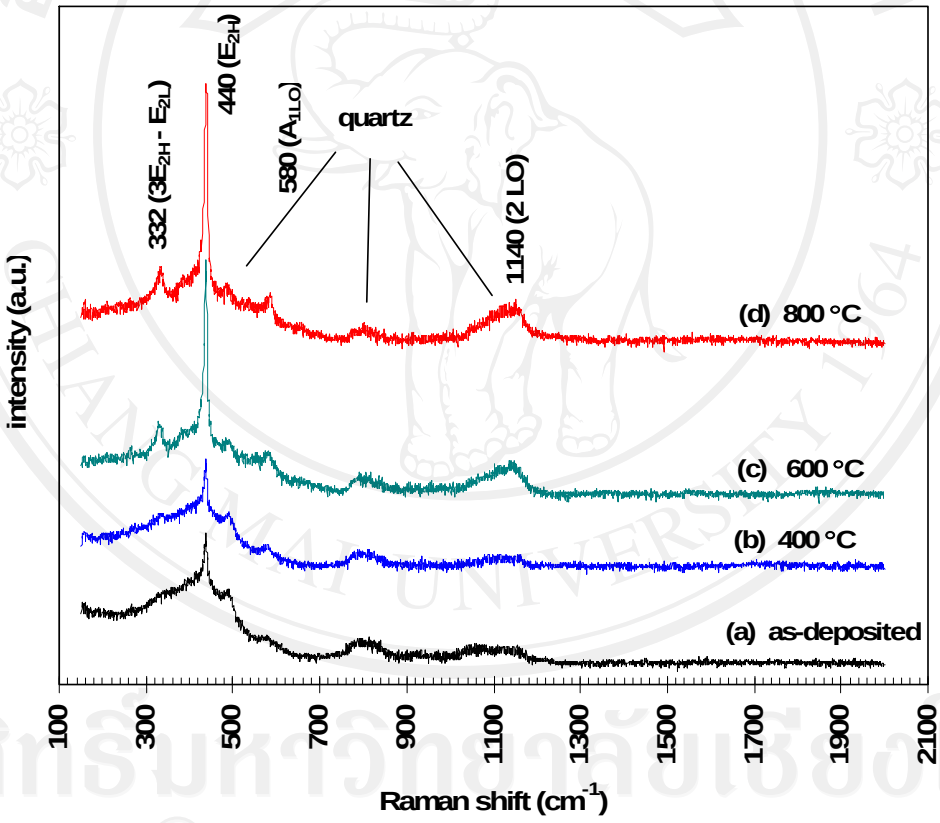

Fig. 4.17 Raman spectra of ZnO thin films of ZnO thin films of (a) the as-deposited sample and the samples annealed at (b) 400 °C, (c) 600 °C, and (d) 800 °C.

4.2.6 Ionoluminescence

IL spectra of ZnO thin films at room temperature consist of two emission bands as shown in fig. 4.18. The green emissions were observed at 483 nm for the as-deposited and the annealed samples at 400 and 600 °C, but 520 nm for the annealed sample at 800 °C. In contrast, the orange-red peaks were observed at 650 nm for all samples. The green band is known as a result of the singly ionized oxygen vacancies [64] whereas the orange-red band corresponds to the excess oxygen atoms (oxygen interstitials) [65], the radiative centre levels of oxygen vacancies were shown in fig. 4.18. It is noted that as the annealing temperature increased from 400 to 600 °C, both emission intensities increased. However, for the sample annealed at 800 °C, the green emission peak shifted to a lower energy with increase in its intensity whereas that of the orange-red emission decreased. Because the kinetic energy of atoms in the ZnO lattice was relatively high at high annealing temperature, the escape rate of oxygen atom was greater than the adsorption rate. Consequently, high oxygen vacancies favorably formed in the ZnO lattice.

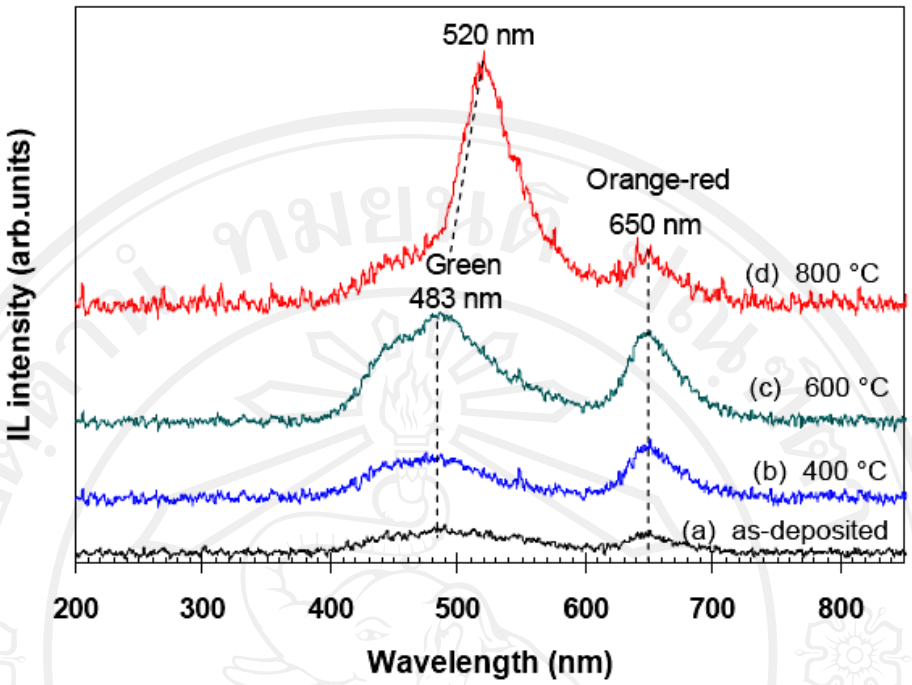

Fig. 4.18 Ionoluminescence spectra of ZnO thin films of (a) the as-deposited sample and the samples annealed at (b) 400 °C, (c) 600 °C, and (d) 800 °C.

Oxygen vacancies (V_o) are the most widely accepted mechanism for the visible emission of ZnO. They can occur in three charge states: the doubly ionized oxygen vacancy V_o^{++} which does not capture any electrons and is doubly positive charged relative to the lattice of ZnO, the singly ionized oxygen vacancy V_o^{+} which has captured one electron and is singly positive charged relative to the lattice, the neutral oxygen vacancy V_o^{x} which has captured two electrons and is neutral relative to the lattice. According to the levels of these three oxygen vacancies in the energy band of ZnO (see fig. 4.19), the origin of the yellow, green, and blue peaks can be attributed to the recombination of the V_o^{++} trapped center with delocalized electrons close to the conduction band, the electron transition from V_o^{+} centers to the valence band edge, and electron transition from V_o^{x} centers to valence band edge, respectively.

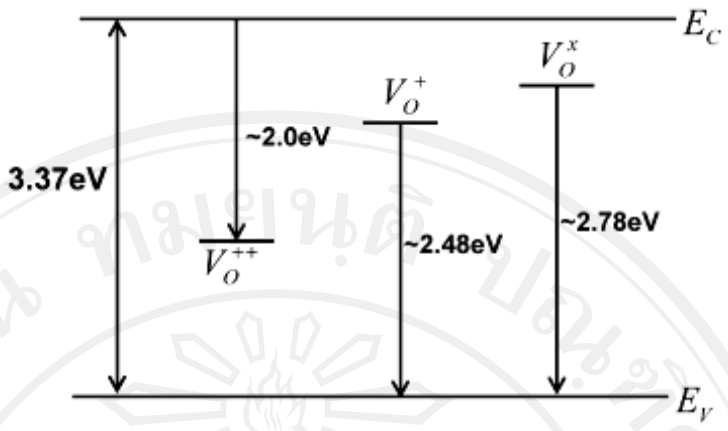

Fig. 4.19 Scheme of the UV emission and the three visible radiative emission processes. [66]

There is a strong indication of the red-shift of the green emission of ZnO. It has been reported that it was due to an increasing of the particle size from 0.7 to 1 nm, which led to the decrease of the E_g [67]. Moreover, the band filling was recently proposed for the red-shift of green emission with aging time [68]. The later was likely to be the reason for the red-shift in this case.

In the case of commercial ZnO phosphors, the oxygen vacancies are distributed in the bulk of the ZnO particles with a narrow energy distribution. In contrast, radiative centres such as oxygen vacancies or other types of defects are within a short distance of the nanoparticle surface. The close proximity of the surface should change their energy and broaden their energy distribution. Based upon a broad trap energy distribution, the wavelength of the green peak from ZnO nanoparticles will decrease when the amounts of electrons recombining at non-radiative centres increase. Increased trapping of electrons on nonradiative centres will result in a decrease of the population of electrons trapped on radiative centres, as shown

schematically in figure 4.20. With less trapping of electrons on radiative centres, the emission intensity would decrease, the wavelength would increase, and the peak breadth would decrease.

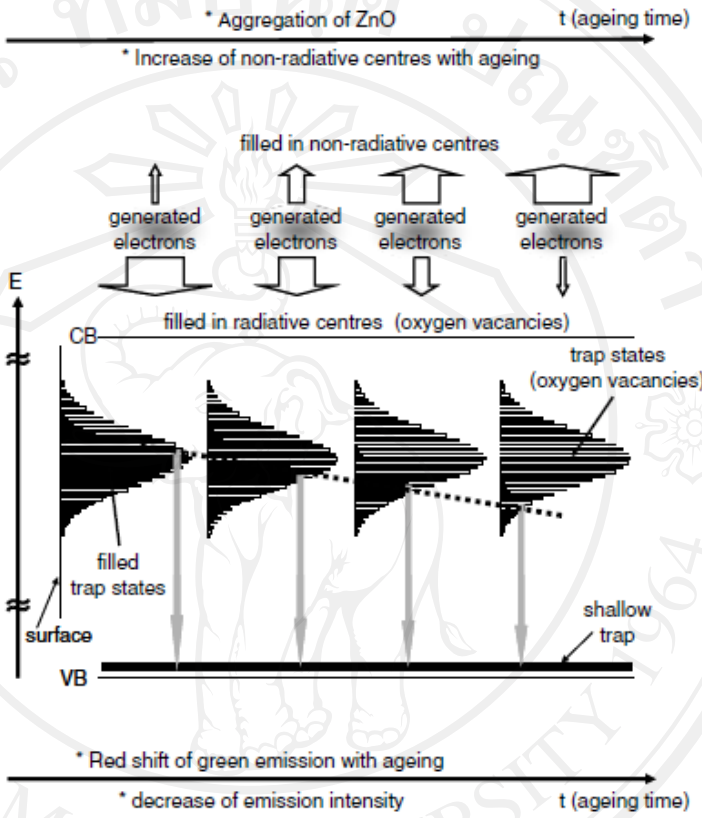

Fig. 4.20 Schematic diagram showing the effects of non-radiative centres and the various filling levels of radiative centres on the intensity and peak wavelength of green emission. In the energy diagram, dark filled areas represent the population of electrons contributing to radiative green emission, and the lengths of the down arrows represent energy of green emission. [68]

4.2.7 Electrical resistivity

Figure 4.21 shows the electrical resistivity and the orange-red emission intensity as a function of the annealing temperature. The resistivity increased from 1.3

to 9.1 kΩ cm with increasing the annealing temperature from 400 to 600 °C. Since, an ideal defect-free ZnO film is an insulator, the well-crystallized sample annealed at 600 °C has high resistivity. However, the annealing treatment at 800 °C decrease the film resistivity as well as the orange-red peak intensity.

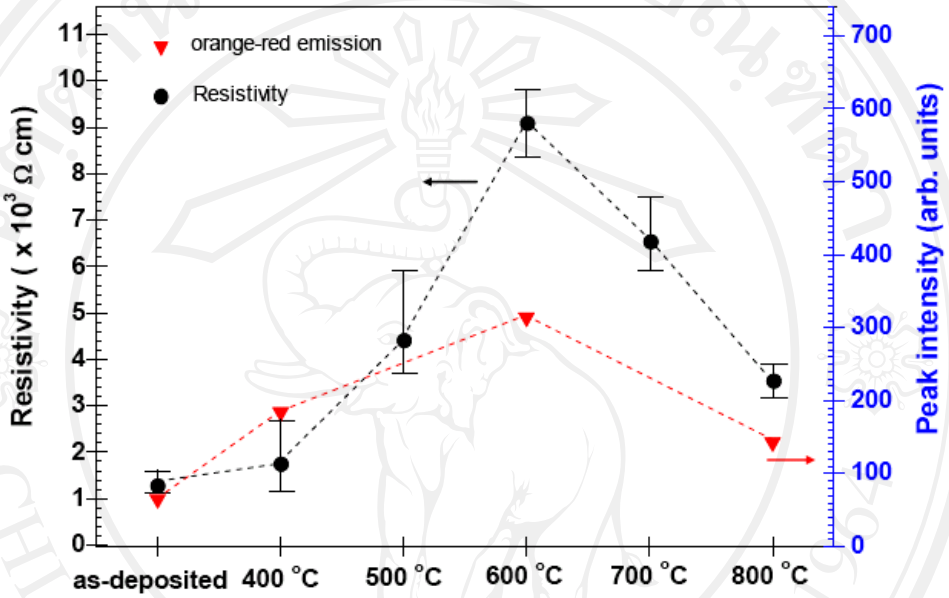

Fig. 4.21 The electrical resistivity and the intensity of orange-red emission of the ZnO films, as functions of the annealing temperature.

4.2.8 Effect of pressure on the size of nanoparticle

Effects of the sparking pressure on the size of nanoparticles were studied under pressure 160-760 torr. Figure 4.22 (a)-(d) shows AFM images of ZnO films prepared under the pressures of 160, 360, 560 and 760 torr, and the average diameters are 16.3, 17.0, 18.1 and 20.5 nm as shown in fig. 4.22, respectively. It is clearly seen that the increase of the sparking pressure increased the diameter of ZnO nanoparticles. Bearing in mind that, the difference of pressure between in and out of the droplet

during the nucleation is one of the parameters which has a strong influence on the size of nanoparticles. The nucleation mechanism of sparking process was discussed in section 4.5.

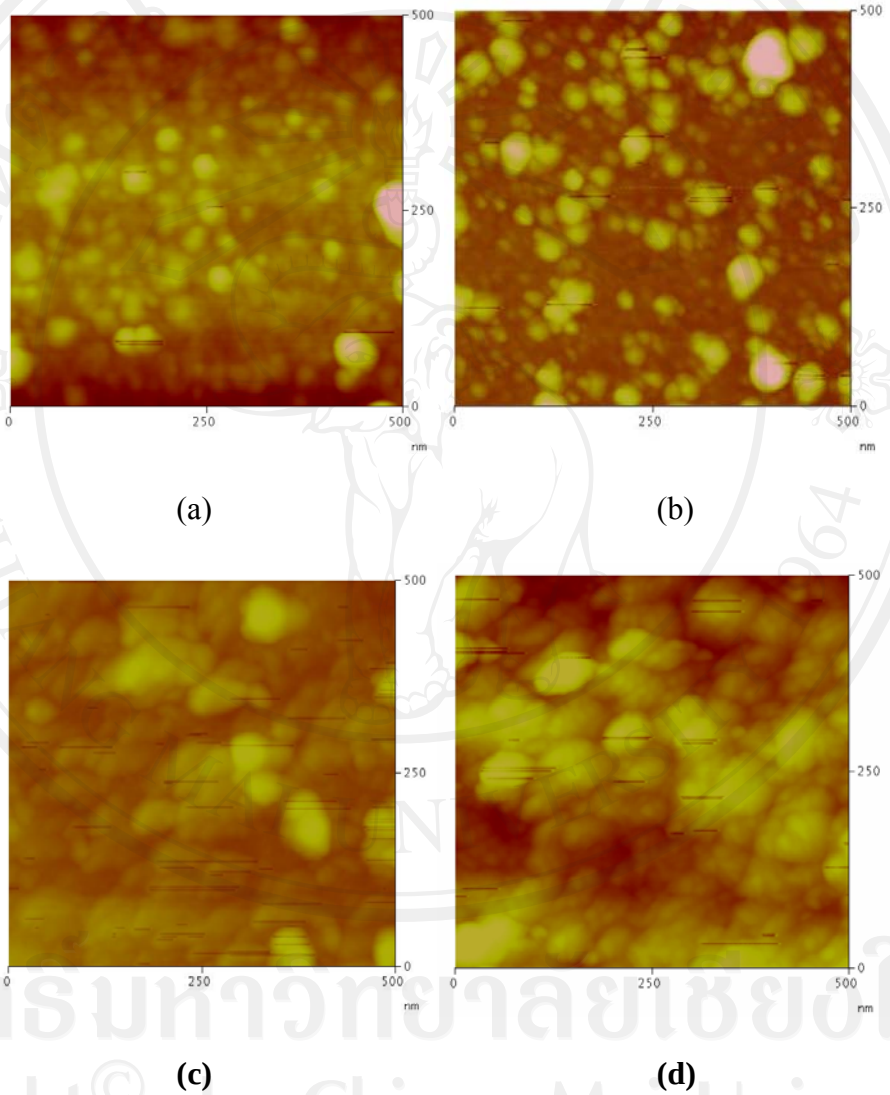

Fig. 4.22 AFM images of ZnO nanoparticles thin films prepared at different pressures: (a) 160 torr, (b) 360 torr, (c) 560 torr and (d) 760 torr.

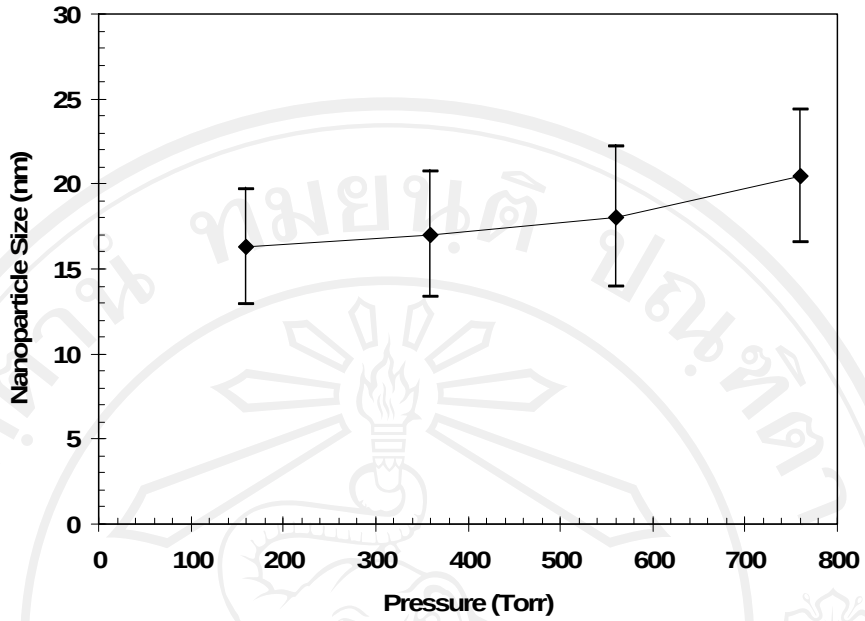

Fig. 4.23 The nanoparticle size of the ZnO samples as a function of the sparking pressure.

4.3 ZnO-TiO_2 coupled nanoparticle thin films

Photocatalytic properties of semiconductor can be improved by adding noble metal or using semiconductor coupled. In principle the coupled of semiconductor oxide seems useful in order to achieve a more efficient electron hole pair separated under the irradiation.

In this part, ZnO-TiO_2 coupled nanoparticle thin films were prepared by sparking process using zinc and titanium wire as the electrodes. The wires were alternated anode and cathode polarity. The ratio of titanium and zinc in the film were measured by EDX. The ZnO-TiO_2 films were annealed at 600 °C, the optimum temperature to improved crystallization of the sparking ZnO thin films [51], for 1 hour in air atmosphere. The crystal structure and compound component of the films

were investigated by XRD and Raman spectroscopy. The photocatalytic activity of the films was determined by the absorption spectra of methylene blue.

4.3.1 Surface morphology and cross-section as SEM images

The SEM image of ZnO-TiO_2 nanoparticulate thin films is shown in fig. 4.24 (a). The elemental homogeneity was further examined by EDX mapping as shown in figs. 4.24 (b) and (c). Zinc and titanium elements are randomly embed in the whole films. Figs. 4.25 (a) and (b) represent EDX mappings and spectra of Zn and Ti elements, respectively. The images indicate the homogeneous distribution of the Zn and Ti elements. Moreover, EDX was used to measure the Zn/Ti atomic ratio. The average atomic Zn:Ti ratios are 5:1 and 6:1 for anode and cathode Ti tip samples, respectively.

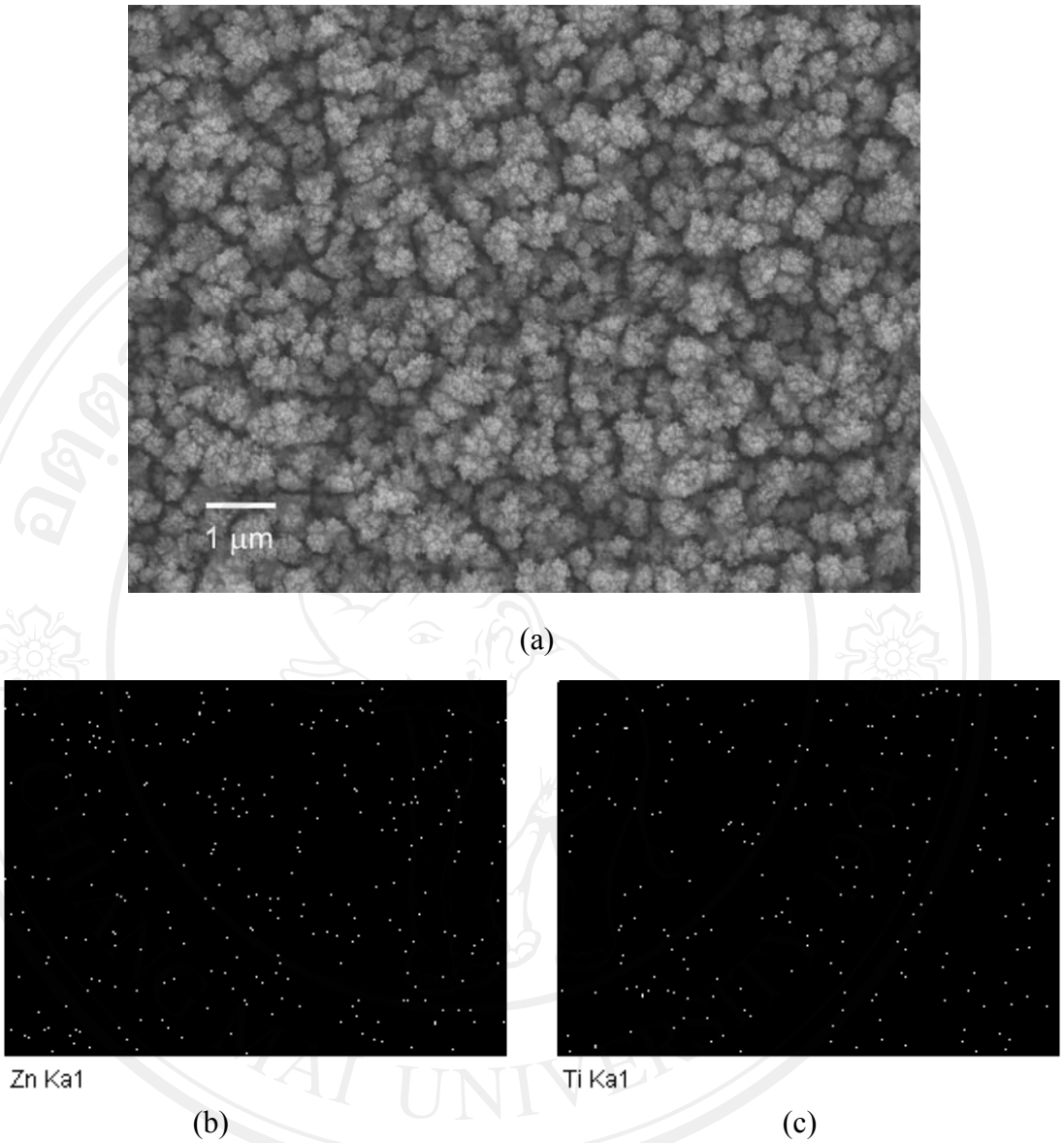

(a)

(b) (c)

Fig. 4.24 (a) SEM images of the as-deposited ZnO-TiO_2 thin films and, (b) and (c) are EDS mapping of zinc and titanium, of (a), respectively.

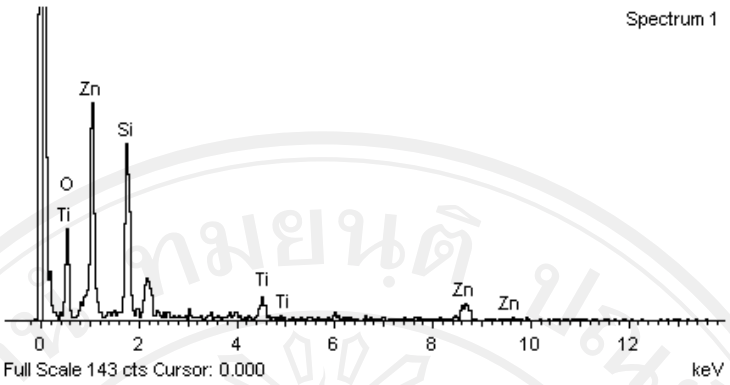

(a)

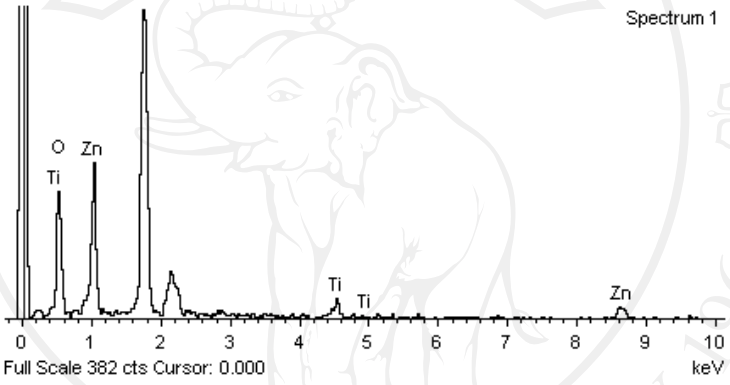

(b)

Fig. 4.25 EDX spectra of (a) cathode titanium and (b) anode titanium.

Fig. 4.26 shows SEM cross-section image of the anode Ti tip sample the film after 100-400 times of sparking. The film deposition rate by sparking process, the tips were 3 mm gap and 2 mm above the substrate and spark at 10 kV was approximately 0.7 nm/spark.

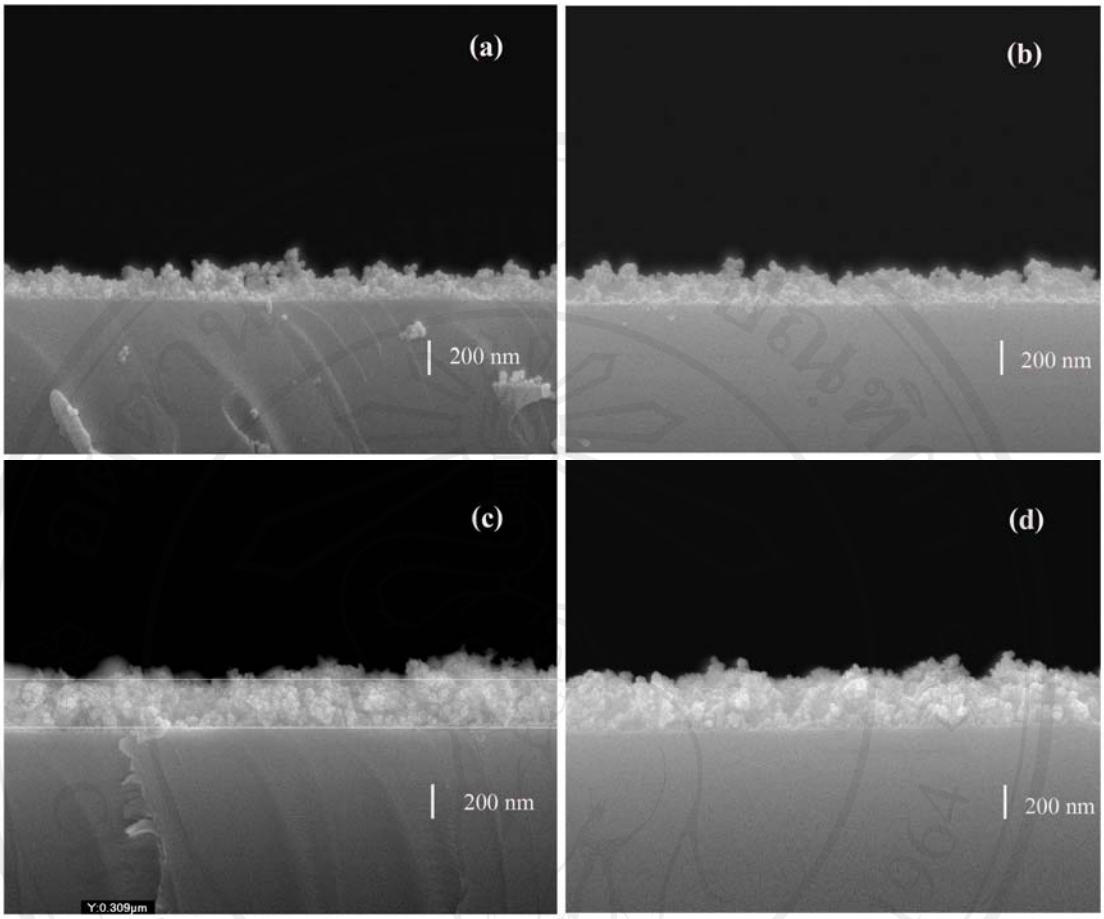

Fig. 4.26 SEM cross section images of the ZnO-TiO_2 films sparking number of (a) 100 times, (b) 200 times, (c) 300 times and (d) 400 times.

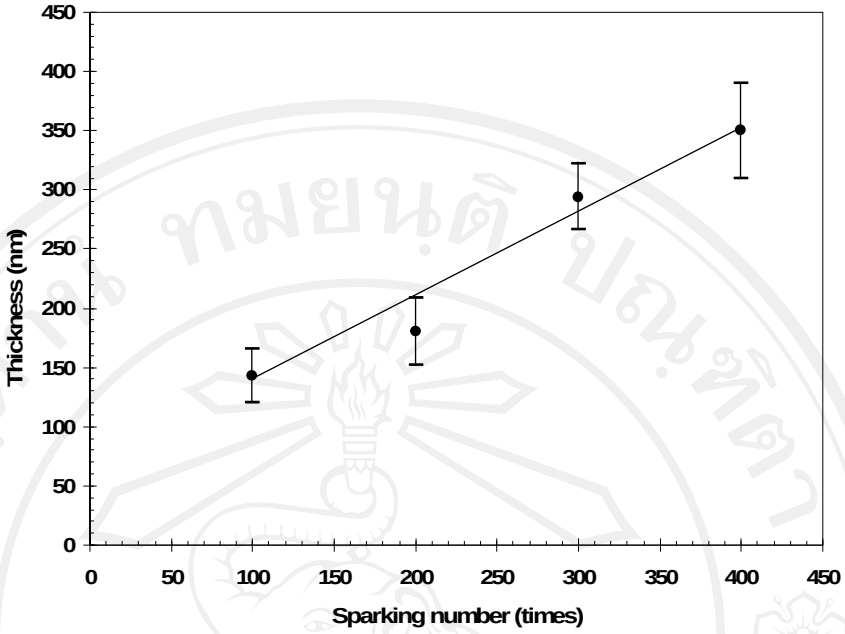

Fig. 2.27 The thickness of the ZnO-TiO_2 thin films as a function of the sparking numbers.

4.3.2 X-Ray diffraction

XRD patterns the as-deposited and annealed at 600 °C of ZnO-TiO_2 films are shown in fig. 4.28. The diffraction peaks of ZnO, α-Zn_2TiO_4(T), Zn_2TiO_4(C), rutile and anatase TiO_2 phases were observed corresponding to JCPDS No.89-1397, 25-1164, 18-1487, 87-0710 and 78-2486, respectively (see vertical bars). For the as-deposited samples, the obtain films are almost in an amorphous state. Upon subsequently annealing treatment crystallization improves. The XRD results show that during the nanoparticle nucleation, the crystals are randomly formed.

It is clearly evident from the diffraction for the ZnO-TiO_2 films, ZnO and zinc titanate are the main component in the films, and therefore, rutile and anatase TiO_2 are small amount component.

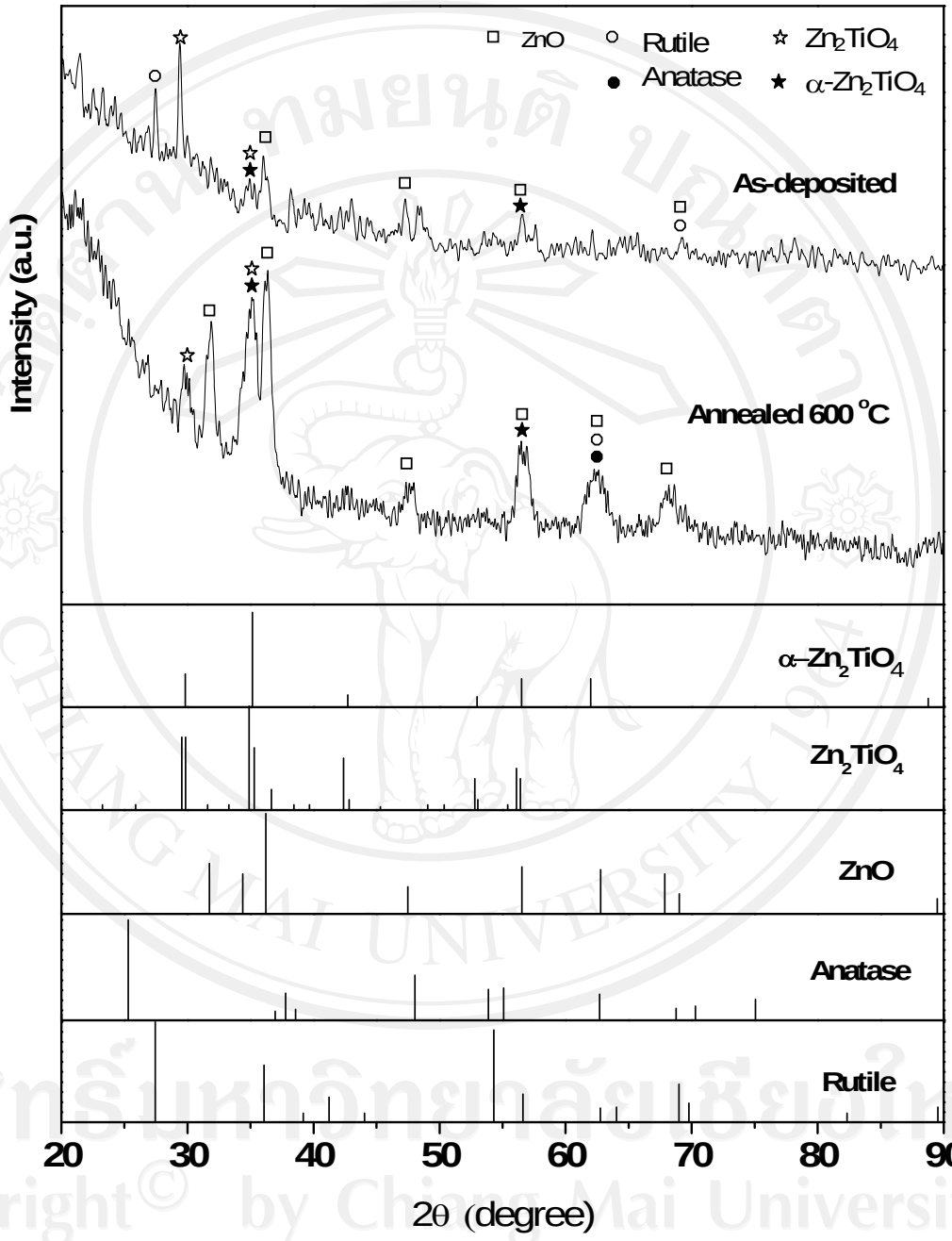

Fig 4.28 XRD patterns of the as-deposited and the annealed at 600 °C $ZnO\text{-}TiO_2$ films.

4.3.3 Raman spectroscopy

Figure 4.29 shows the Raman spectra of ZnO-TiO_2 coupled nanoparticled thin films with an excitation of 514.5 nm line of argon ion laser at room temperature. For the as-deposited films, the spectrum intensities are low due to a lot of amorphous components in the films. There are four peaks being investigated, i.e. Zn_2TiO_4, $3E_{2H}$-E_{2L}, E_2 high and A_{1LO} of ZnO located at 266, 341, 440 and 577 cm^{-1}, respectively. For the annealed samples, the Raman peaks at 720 cm^{-1} is the A_{1g} Raman active mode of Zn_2TiO_4 [69]. In addition, the peaks located at 519 and 246 cm^{-1} corresponds to the B_{1g} of the anatase and multi phonon rutile TiO_2 [70], respectively.

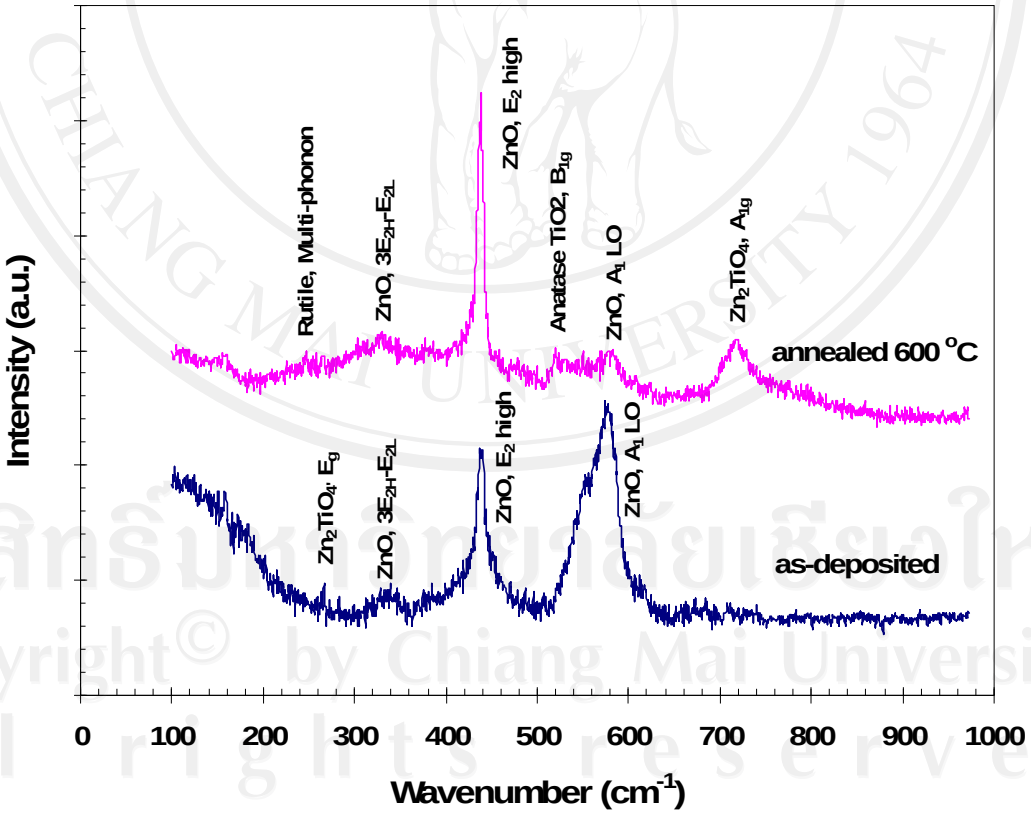

Fig. 4.29 Raman spectra of the as-deposited and the annealed at 600 °C ZnO-TiO_2 coupled nanoparticle thin films.

4.3.4 Ionoluminescence

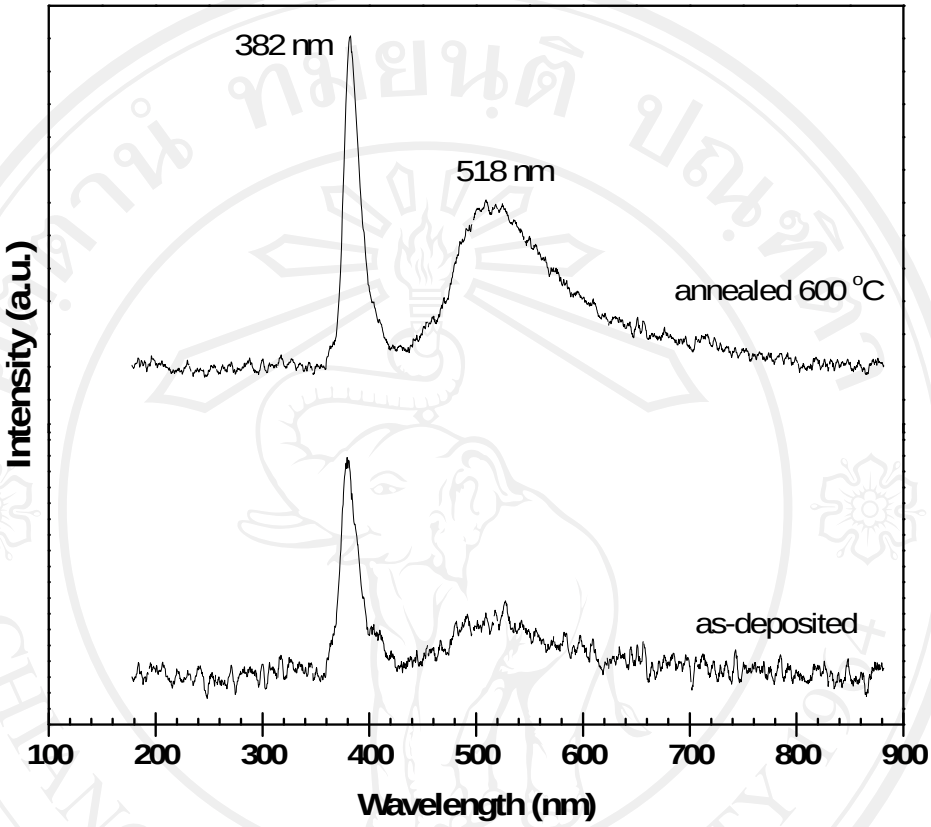

Fig. 4.30 IL spectrum of the as-deposited and the annealed ZnO-TiO_2 films**.**

Both annealed and as-deposited IL spectra of ZnO-TiO_2 thin films at room temperature presents the emission of ZnO which is shown in Fig. 4.30. There are a stronger peak at 382 nm and a weaker board peak around 520 nm which are commonly known to be of the emission spectra of ZnO. The UV emission is near band-edge emission with generated by the free-exciton recombination and green emission (known to be deep-level emission) is the result of the singly ionized oxygen

vacancies**.** Furthermore, the annealed sample is better crystallization than the as-deposited.

4.3.5 UV-vis spectra

The optical transmittance of ZnO-TiO_2 thin films was shown in fig. 4.31. It can be seen that the spectrum has very high transparent invisible region (over 90%) and a sharp drop at around 390 nm. This behaviour is appropriate to used in UV-shielding application.

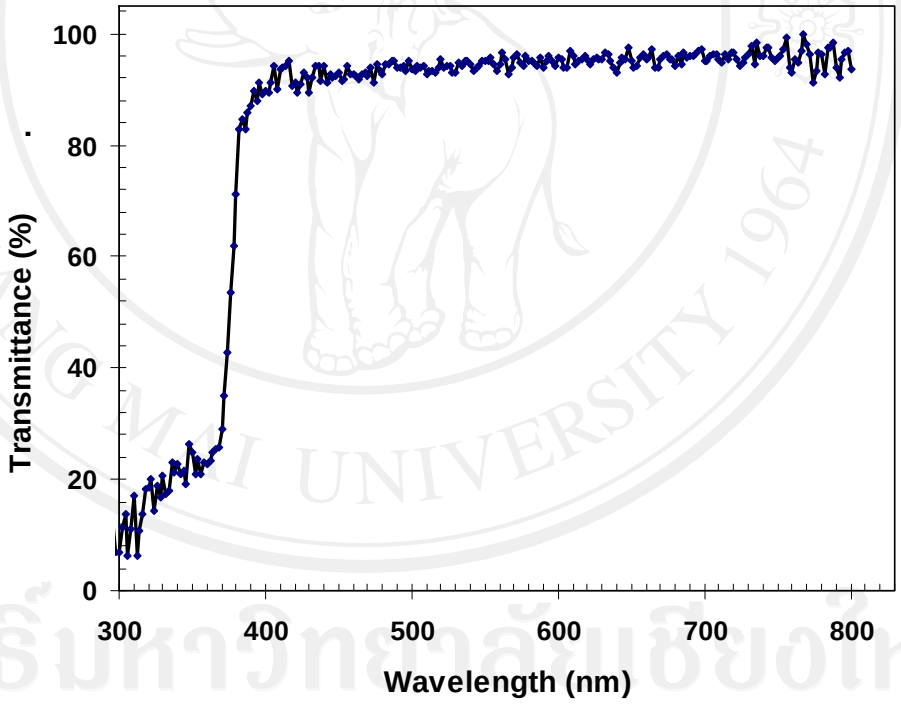

Fig. 4.31 UV-vis transmittance spectrum of the annealed ZnO-TiO_2 films.

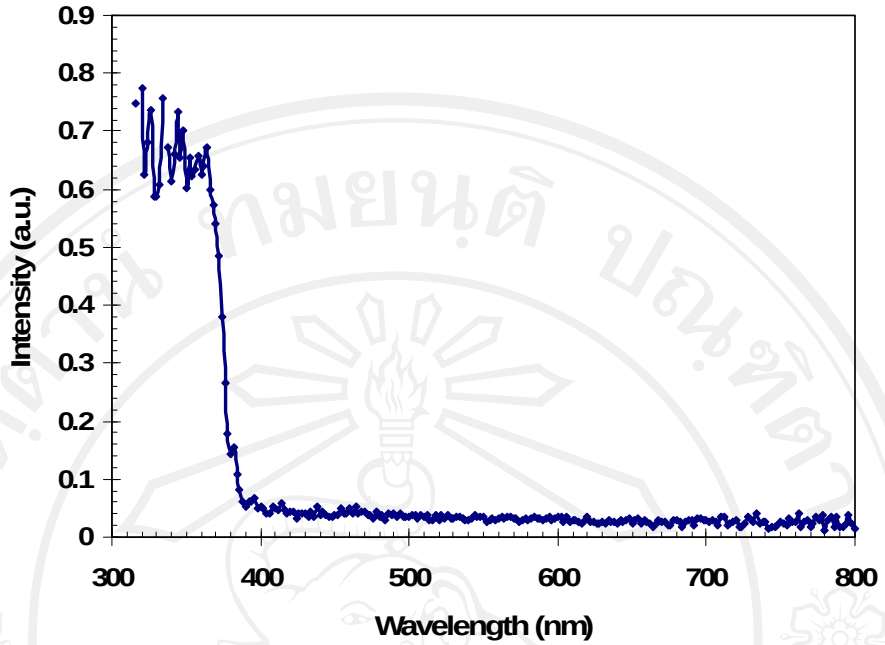

Fig. 4.32 UV-vis absorbance spectrum of the annealed ZnO-TiO_2 films.

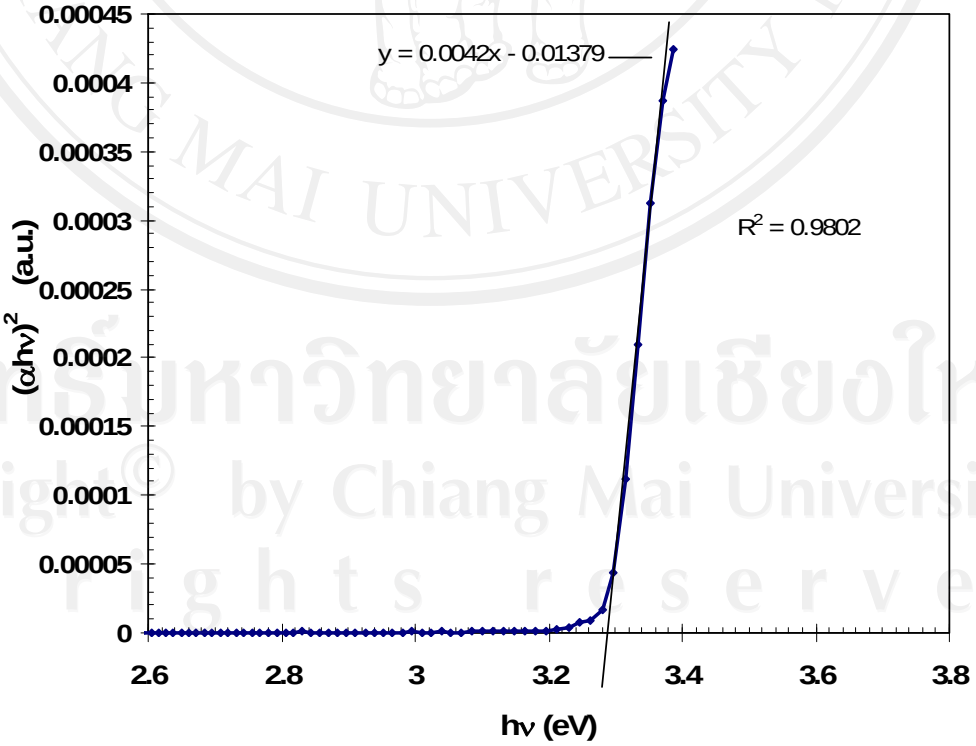

Fig. 4.33 The plot of $(\alpha h\nu)^2$ versus $h\nu$ for estimation of the energy gap (α = ln 1/T).

The optical band gap of the ZnO-TiO_2 films were determined by taking a plot of $(\alpha h\nu)^2$ versus $h\nu$, where α is the absorbance coefficient and $h\nu$ is the photon energy. The band gap energy of the films was found to be 3.28 eV.

4.3.6 Photocatalytic activity

For comparison of photocatalytic activities of the sparking ZnO, TiO_2 and coupled ZnO-TiO_2, the films were sparked 3600 times (4h) and then annealed in air at 600 °C. The films were dipped in 10 μM 500 μl methylene blue solution and irradiated under the sun light for 75 min. The absorption peak around 665 nm indicates amount of MB in solution as shown in fig, 4.34. From these results, the ZnO and TiO_2 thin films are better photocatalytic than the coupled ZnO-TiO_2 because there are a lot of zinc titanate, non-photocatalyst, component in the coupled film. In order to further improve this property, one time of the sparking should use the same metal wires, zinc or titanium, in both electrodes and alternates metals in the next spark. That probably produces the mixer of ZnO and TiO_2, layer by layer, which is suitable for use as coupled photocatalyst.

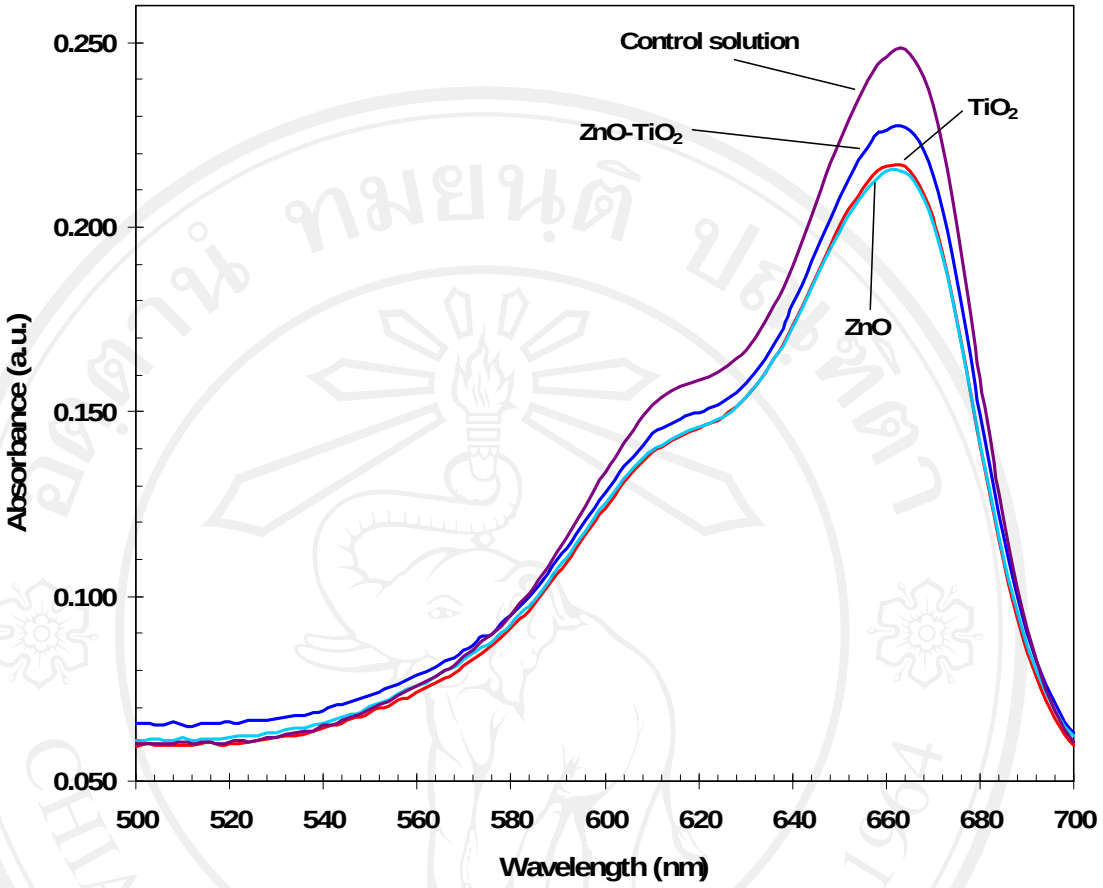

Fig. 4.34 UV–vis adsorption spectra of pure 10 μM methylene blue solution and the solution with dipping ZnO, TiO_2, and ZnO-TiO_2 film under sun light irradiation for 75 min.

The sparks in chapter 4.1-4.3, the sparking voltages were discharged from capacitor. To study effect of sparking pulse, square wave pulse were used as sparking voltage and the results were shown in section 4.4.

4.4 Sparking ZnO using square wave pulse

The ZnO films were deposited on zinc substrate using sparking process in order to achieve light emission by electroluminescence. Samples are processed from 0.62 mm thick substrate and two zinc wire tips. The tips were then placed horizontally at 2 mm spacing and 2 mm above the centre of the substrate. The 10 kV 100 Hz 50% duty cycle pulses, generated by function generator and amplified by high voltage amplifier, were applied between the tips and the sparking occurred.

The experiments were done for 2 hours in stagnant clean and without humidity air at atmospheric pressure and then some annealed at 200, 250, 300 and 350 °C in air for 30 minutes. Ag was used as electrical contacts which connect to the spark and unspark areas for the I-V curve measurement.

4.4.1 Surface morphology and cross-section as imaged by SEM

Figure 4.35(a) shows SEM image of sparking ZnO and its cross-section images were shown in figure 4.36 (b). ZnO is scale-like shape and cover whole substrate surfaces. The film thickness is around 20 μm.

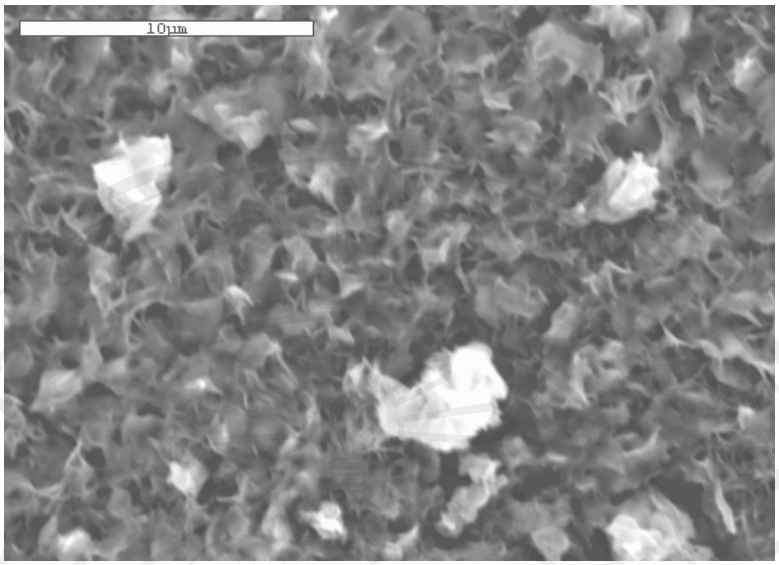

(a)

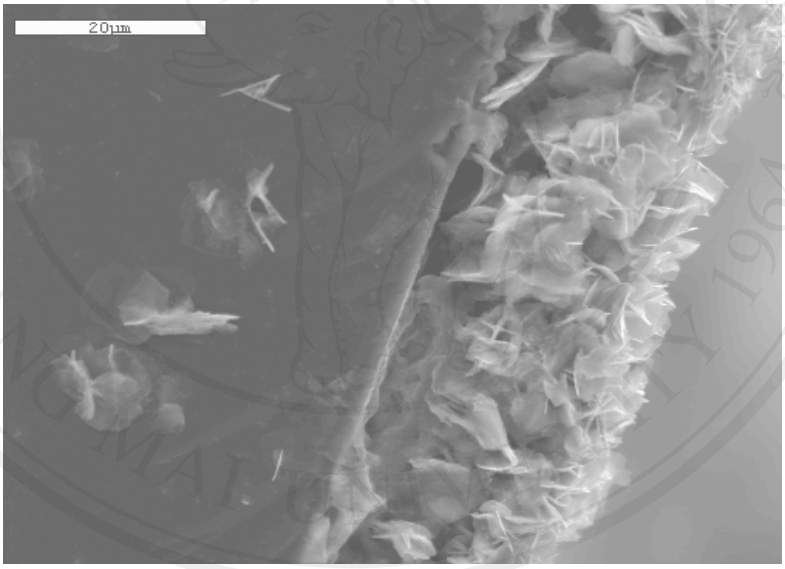

(b)

Fig. 4.35 (a) SEM image of square wave pulse sparking ZnO and (b) cross-section of fig. (a).

4.4.2 I-V characteristics

The current – voltage relation of sparking ZnO on zinc substrate was measured where the silver paint was used as electrical contact. The measurement used voltage

control method, where a constant voltage was applied and the current flow was measured. The results are shown in fig. 4.37. Most samples, except the virgin zinc, can be assumed to behave like diodes showing a clear rectifying behavior of rectifier contact from ZnO and silver contacts.

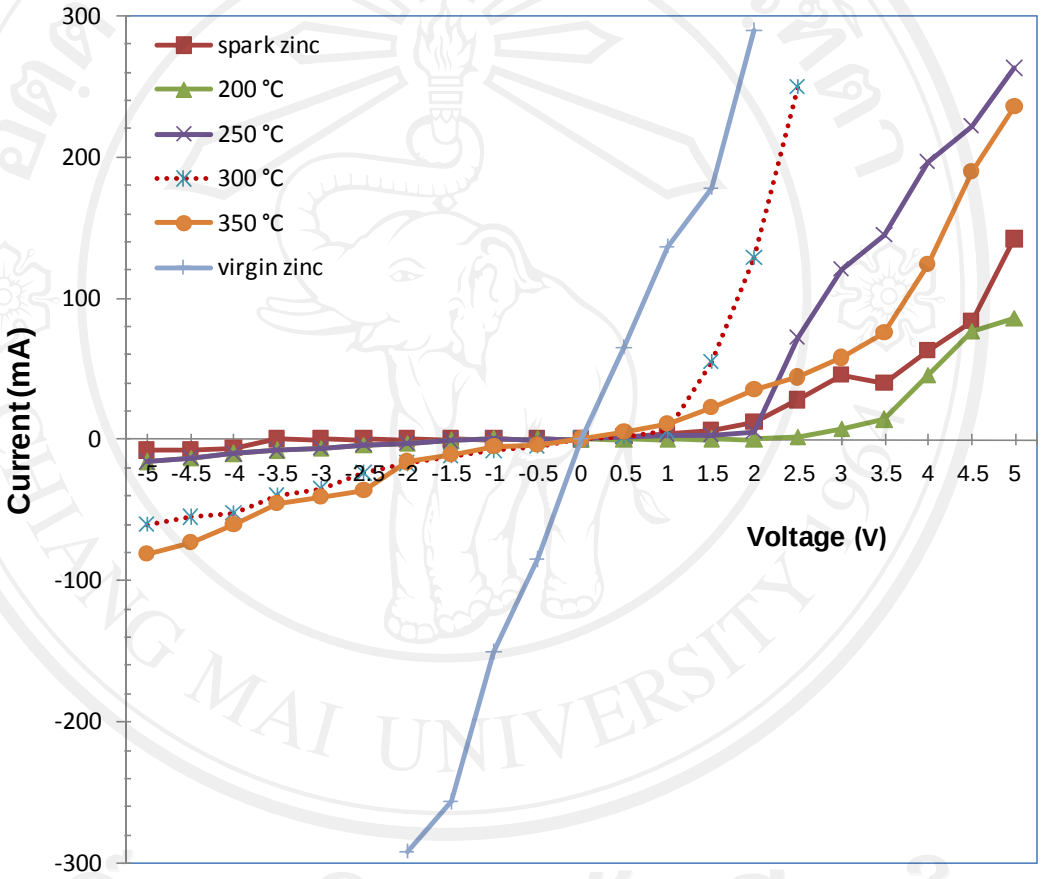

Fig.4.36 I-V curve of sparking ZnO based electroluminescence device as a function of annealing time**.**

Work function (Φ) values of silver, zinc and ZnO are 4.7, 4.3 and 4.45 eV, respectively. The rectifying contacts between silver and ZnO, ($\Phi_{Metal} > \Phi_{n\text{-type semiconductor}}$), can be used to explain these phenomena**.** When a metal and a n-type

semiconductor are connect to a d.c. source. At first, the metal is assumed to be connected to the negative terminal of a battery. As a result, the metal is charged even more negatively than without bias. Thus, the electrons in semiconductor are repelled even more, and potential barrier is increased. Further, the depletion layer becomes wider. Because both barriers are now relatively high, the diffusion currents in both directions are negligible. However, the small and essentially voltage-independent drift current still exists, which results in a very small and these exists net electron current from the metal to the semiconductor (figure 2.8).

If the polarity of the battery is reversed, the potential barrier in the semiconductor is reduced, i.e., the electrons are driven across the barrier so that there is a large net current flowing from the semiconductor into the metal.

4.5 Nucleation mechanism of sparking process

In order to understand a nucleation mechanism of the nanoparticle (NP) formation, the Zn tip was observed during the sparking under an optical microscope. Interestingly, we found that the Zn tip was melting. The bombardment of high-energy electrons accelerated by a high voltage across the Zn sharp tip and the Zn wire, as shown in fig. 4.38, caused high temperature and pressure on molten Zn at the tip surface. Hence, Zn nanodroplets were nucleated, which moved towards the substrate by the high kinetic energy and oxidized in atmospheric air. The particle size of the nanodroplet can be described thermodynamically with the Young–Laplace equation, i.e.

$$\Delta P = 2\gamma/r \qquad (4.1)$$

where r is the radius of curvature, γ is surface free energy of the molten Zn and ΔP is the pressure difference between inside (P_{in}) and outside (P_{out}) the droplet.

Therefore, at a higher applied voltage, the nanoparticle deposited has a smaller average size. In other words, the average particle size can be varied by adjusting strength of the applied voltage because a high specific surface energy is governed by the associated energy stored in such a system [71]. Since the electric energy stored in a capacitor is $E = \frac{1}{2} CV^2$, by sparking at higher voltage the tip has transferred higher energy. This supports that the lower mean sizes of the nanoparticle were successfully deposited at the higher voltages.

Furthermore, the average particle size can be decreased by increasing the local electric field (E_{local}) at the Zn tip, as the fields at the sharp tips are more enhanced by the field enhancement factor (β) than at the dull tip.

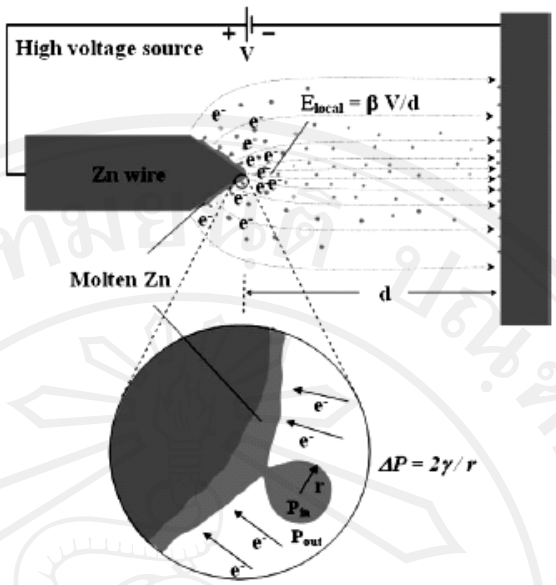

Fig. 4.37 Schematic diagram of the nucleation mechanism of ZnO nanoparticle deposited by the sparking method [51].

By observing the voltage across the sparking gap, three key regions were indentified. Much of the voltage drop occurs across two invisibly thin regions directly adjoining the anode and cathode, which are referred to as the anode drop region and cathode drop region respectively.

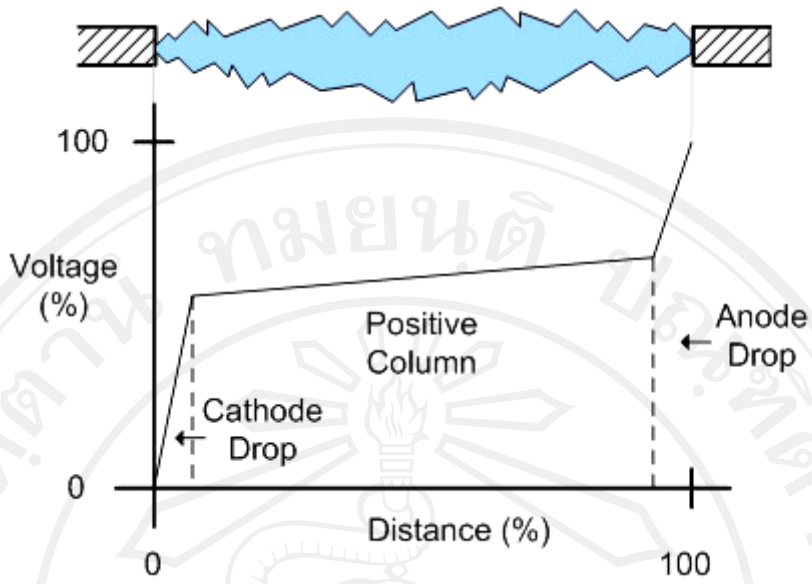

Fig. 4.38 Voltage distribution as function of distance into spark [72]

For a given current through a spark, the power dissipated in the cathode drop region (cathode drop voltage) serves to heat the cathode and cause it to emit electrons, the power dissipated in the anode drop region (anode drop voltage) goes to heating the anode by electron bombardment. The electrons transferred thermal energy to the anode tips. This process produced metallic ions as result more anode erosions than the cathodes.